https://doi.org/10.5194/cp-2019-159
Preprint. Discussion started: 14 January 2020

Climate of the Past Discussions

Mysteriously high $\Delta^{14}C$ of the glacial atmosphere: Influence of ^{14}C production and carbon cycle changes

Ashley Dinauer[1,*], Florian Adolphi[1,2], Fortunat Joos[1]

[1]Climate and Environmental Physics, Physics Institute and Oeschger Centre for Climate Change Research, University of Bern, Sidlerstrasse 5, 3012 Bern, Switzerland
[2]Quaternary Sciences, Department of Geology, Lund University, Sölvegatan 12, 22362 Lund, Sweden
*To whom correspondence should be addressed. Email: ashley.dinauer@climate.unibe.ch

Abstract. Despite intense focus on the ~190 permil drop in atmospheric $\Delta^{14}C$ across the deglacial "mystery interval", the specific mechanisms responsible for the apparent $\Delta^{14}C$ excess in the glacial atmosphere have received considerably less attention. The computationally efficient Bern3D earth system model of intermediate complexity, designed for long-term climate simulations, allows us to address a very fundamental but still elusive question concerning the atmospheric $\Delta^{14}C$ record: How can we explain the persistence of relatively high $\Delta^{14}C$ values during the millennia after the Laschamp event? Large uncertainties in the pre-Holocene ^{14}C production rate, as well as in the older portion of the $\Delta^{14}C$ record, complicate our qualitative and quantitative interpretation of the glacial $\Delta^{14}C$ elevation. Here we begin with sensitivity experiments that investigate the controls on atmospheric $\Delta^{14}C$ in more idealized settings. We show that the long-term process of sedimentation may be much more important to the simulation of $\Delta^{14}C$ than had been previously thought. In order to provide a bounded estimate of glacial $\Delta^{14}C$ change, the Bern3D model was integrated with five available estimates of the ^{14}C production rate as well as reconstructed and hypothesized paleoclimate forcing. Model results demonstrate that none of the available reconstructions of past changes in ^{14}C production can reproduce the elevated $\Delta^{14}C$ levels during the last glacial. In order to increase atmospheric $\Delta^{14}C$ to glacial levels, a drastic reduction of air-sea exchange efficiency in the polar regions must be assumed, though discrepancies remain for the portion of the record younger than ~33 kyr BP. We end with an illustration of how the ^{14}C production rate would have had to evolve to be consistent with the $\Delta^{14}C$ record, by combining an atmospheric radiocarbon budget with the Bern3D model. The overall conclusion is that the remaining discrepancies with respect to glacial $\Delta^{14}C$ may be linked to an underestimation of ^{14}C production and/or a biased-high reconstruction of $\Delta^{14}C$ over the time period of interest. Alternatively, we appear to still be missing an important carbon cycle process for atmospheric $\Delta^{14}C$.

1 Introduction

The cosmogenic radionuclide radiocarbon (^{14}C) is a powerful tracer for the study of several ocean processes including deep ocean circulation and ventilation. Past changes in atmospheric $^{14}C/C$ (i.e., $\Delta^{14}C$, in permil; corresponding to Δ from Stuiver and Polach, 1977), as recorded in absolutely dated tree rings, plant macrofossils, speleothems, corals,

https://doi.org/10.5194/cp-2019-159
Preprint. Discussion started: 14 January 2020

and foraminifera, have been interpreted as possibly reflecting real changes in the ocean's large-scale overturning circulation (Siegenthaler et al., 1980). The extended 54,000-year record of atmospheric $\Delta^{14}C$ from the latest IntCal compilation (i.e., IntCal13; Reimer et al., 2013) and from two Hulu Cave stalagmites (Cheng et al., 2018) suggests that large millennial-scale variations in $\Delta^{14}C$ have occurred during the last glacial, compared to the relatively small (~30 ppm) change in atmospheric CO_2 over the same time period (Fig. 1). When interpreting the implications of such changes, it is important to note that atmospheric $\Delta^{14}C$ is controlled not only by global carbon cycle processes but also by variations in the atmospheric ^{14}C production rate. Therefore, the use of atmospheric $\Delta^{14}C$ as an indicator of past oceanic conditions, particularly those associated with air-sea exchange efficiency and deep ocean ventilation rates, requires reliable estimates of the ^{14}C production rate over time.

The vast majority of all ^{14}C production changes are the result of either solar or geomagnetic modulation of the cosmic ray flux reaching the Earth (Masarik and Beer, 1999; Poluianov et al., 2016). Fig. 1 shows several different proxy records of the global production rate of ^{14}C in relative units covering the full range of the ^{14}C dating method, based on geomagnetic field data from marine sediments (Laj et al., 2000; Laj et al., 2004; Nowaczyk et al., 2013; Channell et al., 2018) and on ^{10}Be and ^{36}Cl measurements in polar ice cores (Adolphi et al., 2018). A fundamental difference between these reconstruction methods is that paleointensity-based estimates of the ^{14}C production rate, by definition, do not reflect changes in the solar modulation of the cosmic radiation, whereas ice-core ^{10}Be-based estimates give the combined influence of solar and geomagnetic modulation on radionuclide production. Of note is the striking coherence in all three records ($\Delta^{14}C$, paleointensity-based production, and ice-core ^{10}Be-based production) of the Laschamp excursion (~41 kyr BP), when the Earth's geomagnetic dipole field briefly reversed and its intensity was close to zero (Nowaczyk et al., 2012; Laj et al., 2014). According to reconstructions and production rate models, this large geomagnetic event caused a doubling of the ^{14}C production rate, leading to the highest $\Delta^{14}C$ values over the last 54 kyr. Relatively high $\Delta^{14}C$ values continued until ~25 kyr BP, then gradually diminished to preindustrial levels, interrupted by a sharp drop in $\Delta^{14}C$ during the so-called "mystery interval" ~17.5 to 14.5 kyr BP (coincident with Heinrich Stadial 1 [HS1]; Broecker and Barker, 2007). While the Laschamp geomagnetic excursion appears to be responsible for the $\Delta^{14}C$ peak at ~41 kyr BP, the production rate estimates during much of the pre-Holocene period are subject to considerable uncertainty.

Paleointensity-based reconstructions are sensitive to coring disturbances of unconsolidated sediments. The last 50 kyr are represented by the uppermost, relatively slushy centimeters of marine sediment cores (Channell et al., 2018). Channell et al. (2018) used only highly accumulating sites and different coring equipment so as to avoid some of these problems, and reached very different conclusions than, e.g., Laj et al. (2000). Similarly, ice-core ^{10}Be records are affected by changes in the transport and deposition of ^{10}Be, which may overprint the production rate changes (e.g., Heikkilä et al., 2013). Furthermore, in order to calculate the ice-core ^{10}Be deposition fluxes, snow accumulation rates must be known for each specific ice core, which themselves have uncertainties on the order of 10 to 20 percent that propagate into the ice-core ^{10}Be fluxes (Gkinis et al., 2014; Rasmussen et al., 2013). The large uncertainties associated with the reconstruction of past changes in ^{14}C production lead to two distinct interpretation problems with respect to

https://doi.org/10.5194/cp-2019-159
Preprint. Discussion started: 14 January 2020

the atmospheric $\Delta^{14}C$ record: (1) the specific mechanisms responsible for high glacial $\Delta^{14}C$ levels, and (2) the extent to which production changes contributed to the deglacial $\Delta^{14}C$ decline.

Earlier model studies have focused heavily on the ~190 permil drop in atmospheric $\Delta^{14}C$ across the mystery interval and on the deglacial trends in $\Delta^{14}C$ after HS1 (Muscheler et al., 2004; Broecker and Barker, 2007; Skinner et al., 2010; Mariotti et al., 2016; Delaygue et al., 2003; Marchal et al., 2001; Huiskamp and Meissner, 2012; Hain et al., 2014). Historically, the younger portion of the $\Delta^{14}C$ record has received more attention than the glacial section because of the early emphasis on the general climatic trends of the North Atlantic stadials (HS1 and the Younger Dryas [YD]) and the Bølling-Allerød (BA) warm period, and on the important role of an exceptionally aged (^{14}C-depleted) deep-water mass in the pulsed rise of atmospheric CO_2 during the last glacial termination (e.g., Skinner et al., 2017). Less research over the last few decades has studied the mechanisms responsible for high glacial $\Delta^{14}C$ levels. The model studies that are available point out the difficulties in simulating the correct glacial $\Delta^{14}C$ levels (Hughen et al., 2004; Köhler et al., 2006). These studies demonstrate with box models that glacial levels of $\Delta^{14}C$ cannot be attained without invoking significant changes in ocean circulation, air-sea gas exchange, and carbonate sedimentation. However, the box models were not able to reproduce $\Delta^{14}C$ values higher than 700 permil, and these results still need to be scrutinized with models of higher complexity. To our knowledge, no three-dimensional ocean biogeochemical model has yet simulated the 50,000-year record of $\Delta^{14}C$. Many questions remain unanswered, in particular: What mechanism can account for the persistence of relatively high $\Delta^{14}C$ values during the millennia after the Laschamp excursion?

The expected time scale for sustaining elevated levels of atmospheric $\Delta^{14}C$ after a production peak is on the order of thousands of years, a time scale tied to the mean lifetime of ^{14}C (~8223 years; Audi et al., 2003; Bé et al., 2013) and the time required for deep ocean ventilation (up to about 1000 years). Specifically, Muscheler et al. (2004) demonstrate that the characteristic time constant for equilibration of $\Delta^{14}C$ after a perturbation in atmospheric production is 5000 years. By this analysis, the Laschamp event, which lasted only about 1500 to 2000 years (Laj et al., 2000), was insufficient to sustain the high $\Delta^{14}C$ values observed over the next ~15,000 years. The lack of significant changes (only ~10 percent) in atmospheric CO_2 during the time period of interest raises the question of what causes variations in atmospheric $\Delta^{14}C$, but not CO_2, on millennial time scales? The obvious answers are: cosmic ray modulation and air-sea gas exchange. Ultimately, no explanation for high glacial $\Delta^{14}C$ levels can be complete in the absence of more robust estimates of the pre-Holocene ^{14}C production rate, as well as a good understanding of the ocean carbon cycle under glacial climate conditions.

One of the major challenges associated with modelling glacial-interglacial climate cycles is that it is currently not possible to reproduce climate and atmospheric CO_2 variations on the basis of orbital forcing alone. Problems include the complexity of the Earth system, making it difficult to represent all the relevant processes in models, and the long time scales involved, making simulations covering tens of thousands of years costly in computation time. Glacial-interglacial simulations with dynamic ocean and land models of intermediate complexity have begun to emerge, but these models are not yet able to reproduce the reconstructed variations in important proxy data or the

https://doi.org/10.5194/cp-2019-159
Preprint. Discussion started: 14 January 2020

timing of CO_2 variations during the last glacial termination (Brovkin et al., 2012; Ganopolski and Brovkin, 2017; Menviel et al., 2012). A wide variety of mechanisms related to the ocean and land carbon cycles including exchange processes with marine sediments, coral reefs, and the lithosphere have been proposed to explain the glacial-interglacial variations in atmospheric CO_2 (Archer et al., 2000; Fischer et al., 2010; Wallmann et al., 2016), but the causes remain elusive. As long as there are still large gaps in our understanding of the glacial climate and associated ocean carbon cycle, a convenient way to examine the impact of the possible mechanisms on atmospheric CO_2 levels, and here on $\Delta^{14}C$, is to perform sensitivity experiments and scenario-based simulations with models. This allows us to investigate specific phenomena in more idealized settings, permitting us to investigate in detail which parameters and processes are most important in controlling atmospheric $\Delta^{14}C$ levels.

In this paper we extend previous modelling efforts concerning the record of atmospheric $\Delta^{14}C$ with respect to three issues: (1) the sensitivity of the $\Delta^{14}C$ response to carbon cycle changes and the potential importance of marine sediments, (2) the simulation of $\Delta^{14}C$ covering the time range of the IntCal13 radiocarbon calibration curve (50,000 years), the primary focus being the explanation of high glacial $\Delta^{14}C$ levels, and (3) a new model-based reconstruction of the ^{14}C production rate for the last 50 kyr as inferred from an atmospheric radiocarbon budget. In the following sections we first introduce the Bern3D earth system model of intermediate complexity and describe the carbon cycle scenarios for forcing it. We then use step changes in the ^{14}C production rate and in selected parameters of the ocean carbon cycle model to gain insight into the transient and equilibrium response of atmospheric $\Delta^{14}C$. After these sensitivity experiments we present the results of paleoclimate simulations forced by available reconstructions of past changes in ^{14}C production together with well-known and hypothesized carbon cycle changes accompanying glacial-interglacial climate cycles. Finally, we present results for a first attempt to reconstruct the history of the ^{14}C production rate using the Bern3D model forced with reconstructed variations in atmospheric $\Delta^{14}C$ and CO_2. We end with a comparison of three fundamentally different (model-based, paleointensity-based, and ice-core ^{10}Be-based) reconstructions of atmospheric ^{14}C production.

2 Materials and methods

2.1 Brief description of the Bern3D model

Simulations are performed with the computationally efficient Bern3D earth system model of intermediate complexity (version 2.0), which is designed for long-term climate simulations over several tens of thousands of years. The Bern3D couples a frictional geostrophic 3-D ocean general circulation model (Edwards et al., 1998; Edwards and Marsh, 2005; Müller et al., 2006), a 2-D energy-moisture balance atmosphere model (Ritz et al., 2011), an ocean carbon cycle model (Müller et al., 2008; Tschumi et al., 2008; Parekh et al., 2008), a chemically active 10-layer ocean sediment model (Heinze et al., 1999; Tschumi et al., 2011; Roth et al., 2014; Jeltsch-Thömmes et al., 2019), and a four-box model representing carbon stocks in the terrestrial biosphere (Siegenthaler and Oeschger, 1987). The coarse-resolution ocean model is implemented on a 41 x 40 horizontal grid, with 32 logarithmically spaced layers in the vertical. The seasonal

https://doi.org/10.5194/cp-2019-159
Preprint. Discussion started: 14 January 2020

Climate of the Past Discussions

cycle is resolved with 96 time steps per year. The tracers carried in this model study include temperature, salinity, dissolved inorganic carbon (DIC), dissolved organic carbon (DOC), carbon isotopes (^{13}C and ^{14}C) of DIC and DOC, alkalinity (ALK), phosphate, silicate, iron, dissolved oxygen (O_2), preformed dissolved oxygen ($O_{2,pre}$), and an "ideal age" tracer. The ideal age is set to zero in the surface layer, increased by Δt in all interior grid cells at each time step of duration Δt, and transported by advection, diffusion, and convection. For a more complete description of the Bern3D model, the reader is referred to Appendix A.

2.2 Implementation of the ^{14}C tracer

Natural radiocarbon (^{14}C) is a cosmogenic radionuclide produced in the atmosphere by cosmic radiation. Once oxidized to $^{14}CO_2$, it participates in the global carbon cycle. Atmospheric $^{14}CO_2$ invades the ocean by air-sea gas exchange, where it is subject to the same physical and biogeochemical processes that affect DIC. The only difference is that ^{14}C is lost by radioactive decay (half-life of 5700 $\pm$ 30 years; Audi et al., 2003; Bé et al., 2013). The governing natural processes, namely, atmospheric ^{14}C production, air-sea gas exchange, physical transport and mixing in the water column, biological production and export of particulate and dissolved matter from the surface ocean, particle flux through the water column, particle deposition on the sea floor, remineralization and dissolution in the water column and the sediment pore waters, and vertical sediment advection and sediment accumulation, are explicitly represented in the Bern3D model (see Fig. 2).

Modelled ^{14}C is often expressed relative to carbon, which is convenient for comparison to radiocarbon measurements which are generally reported as $\Delta^{14}C$. The purpose of $\Delta^{14}C$, i.e., the fractionation-corrected ratio of $^{14}C/C$ relative to that of the AD 1950 atmosphere, is to isolate the effect of radioactive decay. In this study, $\Delta^{14}C$ is treated as a diagnostic variable using the two-tracer approach of OCMIP-2. Rather than modelling only the $^{14}C/C$ ratio, the ^{14}C tracer is carried independently from the carbon tracer. It is normalized by the standard ratio of the preindustrial atmosphere ($^{14}r_{std}$ = 1.170 x 10^{-12}; Orr et al., 2017) in order to minimize the numerical error of carrying very small numbers. It is also fractionation corrected. For comparison to observations, $\Delta^{14}C$ is calculated from the normalized and fractionation-corrected modelled ^{14}C concentration:

$$\Delta^{14}C = 1000\left({}^{14}r' - 1\right) \tag{1}$$

where $^{14}r'$ is the ratio of $^{14}C/C$ divided by $^{14}r_{std}$. The source-minus-sink equation for the atmospheric carbon tracer (i.e., gaseous CO_2) is analogous to that for ^{14}C, except that the equation omits the source–sink terms due to atmospheric production and radioactive decay. With respect to the ocean carbon cycle model, the oceanic carbon tracer sees a constant input of DIC from weathering on land, whereas there is no supply of ^{14}C to the ocean from terrestrial weathering.

https://doi.org/10.5194/cp-2019-159
Preprint. Discussion started: 14 January 2020

In the preindustrial spin-up simulation needed to initialize the Bern3D model, atmospheric CO_2 is held constant at 278.05 ppm and atmospheric $\Delta^{14}C$ at 0 permil. During this integration time the ocean inventories of carbon and ^{14}C adjust to the forcing fields. The resulting changes after >50,000 years of integration are negligibly small. Fig. 3 shows the steady-state $\Delta^{14}C$ distribution in the surface (< 100 m) and deep (> 1500 m) ocean for the preindustrial control run. The large-scale distribution of modelled $\Delta^{14}C$ broadly resembles the observed pattern in the Global Ocean Data Analysis Project (GLODAP; Key et al., 2004). That final state (i.e., the end of the preindustrial spin-up) is used to diagnose the ^{14}C production rate for the preindustrial atmosphere, such that the rate of ^{14}C production is balanced by radioactive decay and the net fluxes out of the atmosphere. For transient simulations, an adjustable scale factor is applied to the preindustrial steady-state value in order to account for production changes induced by solar and/or geomagnetic modulation. The former is derived from, e.g., available reconstructions of the ^{14}C production rate in relative units, as detailed in Sect. 2.5.

2.3 Model configurations

We focus in this paper on the response of atmospheric $\Delta^{14}C$ to changes in ^{14}C production and the ocean carbon cycle. For a deeper mechanistic understanding of the driving processes, step response experiments are first performed (see Sect. 3.1). These simulations include perturbations of the steady-state $^{14}C/C$ distribution under preindustrial conditions. We investigate the impact of step changes in (1) the ^{14}C production rate ("higher production" scenario), (2) wind stress and vertical diffusivity ("reduced deep ocean ventilation" scenario), and (3) the gas transfer velocity ("enhanced permanent sea ice cover" scenario). After a step change at time 0, the simulations are run to near-equilibrium over a 50,000-year integration. The following model configurations and therefore exchanging carbon reservoirs are considered: atmosphere–ocean (OCN), atmosphere–ocean–land (OCN-LND), atmosphere–ocean–sediment (OCN-SED), and atmosphere–ocean–land–sediment (ALL).

Next we examine the influence of changes that are transient in nature. We simulate atmospheric $\Delta^{14}C$ over the full range of the ^{14}C dating method (i.e., 50 to 0 kyr BP) (see Sect. 3.2 and 3.3). These transient simulations are initialized at 70 kyr BP using model configuration ALL, and forced by reconstructed changes in ^{14}C production (see Sect. 2.5) over a 70,000-year integration. The first 20,000 years of the integration are considered a spin-up. Although the full record is simulated, we focus our analysis on the millennial-scale variation in atmospheric $\Delta^{14}C$ before incipient deglaciation at ~18 kyr BP. Eight model runs are carried out for each production rate reconstruction, using different combinations of forcing fields and parameter values as described next.

2.4 Carbon cycle scenarios

In our transient simulations with the Bern3D model, eight scenarios based on different assumptions about the global carbon cycle are considered, the details of which are summarized in Table 1. The goal is to investigate the extent to

https://doi.org/10.5194/cp-2019-159
Preprint. Discussion started: 14 January 2020

which changes in the ocean carbon cycle could explain high glacial $\Delta^{14}C$ levels. We therefore consider a wide range of scenarios, including some extreme cases.

In the first scenario (MOD), the model is run with fixed preindustrial boundary conditions for the Earth's orbital parameters, radiative forcing due to well-mixed greenhouse gases, and ice sheet extent. As a consequence, atmospheric CO_2 remains approximately constant at the preindustrial level of 278.05 ppm over the simulation. The second scenario (PAL) considers reasonably well-known climate forcing over the last glacial-interglacial cycle. Simulations under this scenario are initialized with output from a previous spin-up simulation forced by glacial boundary conditions with respect to orbital parameters (Berger, 1978), greenhouse gas radiative forcing based on reconstructed atmospheric greenhouse gases (Köhler et al., 2017), and ice sheet extent. In simulations under PAL, the model is integrated until 0 kyr BP following the reconstructed histories of the former. Ice sheets for the preindustrial and Last Glacial Maximum (LGM) states are taken from Peltier (1994) and linearly scaled using the global benthic $\delta^{18}O$ stack of Lisiecki and Stern (2016), which is a global ice volume proxy. Changes in the albedo, salinity and latent heat flux associated with the ice sheet buildup or melting are also taken into account (Ritz et al., 2011). Model scenario PAL appears to still be missing an important process or feedback for atmospheric CO_2, as it cannot reproduce the observed low glacial CO_2 level without invoking additional changes (see, e.g., Tschumi et al., 2011; Menviel et al., 2012; Roth and Joos, 2013; Jeltsch-Thömmes et al., 2019).

In this study, we consider six scenarios that invoke additional changes to force the model toward the observed low glacial CO_2 concentration. In addition to the PAL forcing, a time-varying scale factor $F(t)$ is applied to some combination of tunable model parameters: wind stress scale factor τ, vertical diffusivity K_V, gas transfer velocity k_w, $CaCO_3$-to-POC export ratio rr, and POC remineralization length scale ℓ_{POC}. For the preindustrial period, the value of $F(t)$ is fixed at 1, whereas the theoretical LGM value was chosen in order to achieve an atmospheric CO_2 concentration close to the LGM level of ~190 ppm (see Table 1), as determined by sensitivity experiments. Note that the same values of $F(t)$ apply to any of the model parameters considered in a given scenario. To obtain intermediate values, $F(t)$ is linearly scaled using the global benthic $\delta^{18}O$ stack (see Fig. 1). For the spin-up needed to initialize these simulations, the glacial spin-up simulation of PAL was integrated for 50,000 model years, with tunable parameters adjusted to their appropriate glacial values. Atmospheric CO_2 drawdown of up to ~100 ppm is achieved over this 50,000-year integration. From that final spun-up state, the model is run forward in time until 0 kyr BP with PAL and $F(t)$ forcing.

The first of these scenarios (CIRC) allows us to test the sensitivity of the model results with respect to changes in ocean circulation. Tunable model parameters τ and K_V were reduced to 40 percent of their preindustrial values throughout the global ocean during the LGM (i.e., $F_{\tau,K_V} = 0.4$). Such a drastic change in the wind stress field is not realistic. Rather, these changes should be viewed as "tuning knobs" that force the ocean model into a poorly ventilated state with an "older" ideal age and ^{14}C-depleted deep waters, as suggested for the glacial ocean (e.g., Sarnthein et al., 2013). In the model's implementation, a change in wind stress does not affect the gas transfer velocity k_w, unlike in the real ocean where changes in wind stress and wind speed act together. The influence of a change in air-sea exchange

https://doi.org/10.5194/cp-2019-159
Preprint. Discussion started: 14 January 2020

efficiency on the model results was investigated in a second scenario (VENT) where k_w is reduced in the model's north (> 60°N) and south (> 48°S) polar areas in addition to global reductions of τ and K_V ($F_{\tau,K_V,k_w} = 0.4$). A 60 percent reduction of k_w is unlikely to be correct but is a straightforward way to reduce the model's gas exchange efficiency. In the third scenario (VENTx), reduction of polar k_w to 0 percent of its preindustrial value was tested ($F_{\tau,K_V} = 0.4$; $F_{k_w} = 0.0$). Here, k_w remains fixed at 0 percent during the last glacial and is adjusted to its preindustrial value via a linear ramp across the last glacial termination (~18 to 11 kyr BP). In this scenario, sea ice would permanently cover 100 percent of the Southern Ocean during the last glacial, which is not supported by the sea ice reconstructions of Gersonde et al. (2005) and Allen et al. (2011), and also the high-latitude (> 60°N) North Atlantic and Arctic Ocean, for which there is some evidence (Müller and Stein, 2014; Hoff et al., 2016).

We end by investigating the sensitivity of the model results to changes in the parameters controlling the export production of $CaCO_3$ and the water column remineralization of POC. Model scenario BIO considers changes of the $CaCO_3$-to-POC export ratio (and thus also the $CaCO_3$-to-POC rain ratio; Archer and Maier-Reimer, 1994) ($F_{rr} = 0.8$) and POC remineralization length scale (Roth et al., 2014) ($F_{\ell_{POC}} = 1.2$). These changes impact the global carbon cycle by influencing the vertical gradients of DIC, ALK, and nutrients in the water column. A change in the fluxes of POC and $CaCO_3$ to the sea floor drives a change in the magnitude of POC and $CaCO_3$ burial in the sediments. A modest reduction in the export ratio during the last glacial is compatible with reconstructed variations in carbonate ion concentrations (Jeltsch-Thömmes et al., 2019). How the depth of POC remineralization changed over time is still unknown. The last two scenarios consider the combined effect of physical and biogeochemical changes: PHYS-BIO ($F_{\tau,K_V,k_w,rr} = 0.7$) and PHYS-BIOx ($F_{\tau,K_V,k_w,rr} = 0.8$; $F_{\ell_{POC}} = 1.2$).

2.5 Field- and model-based reconstruction of ^{14}C production

Our ability to attribute past changes in atmospheric $\Delta^{14}C$ to climate-related changes in the ocean carbon cycle is limited by our ability to reconstruct a precise and accurate history of the ^{14}C production rate. Past changes in ^{14}C production can be estimated from geomagnetic field reconstructions and from ^{10}Be measurements in polar ice cores. For ice-core ^{10}Be-based estimates, we use the ice-core radionuclide stack of Adolphi et al. (2018), which is based on ^{36}Cl data from the GRIP ice core (Baumgartner et al., 1998), and on ^{10}Be data from the GRIP (Yiou et al., 1997; Baumgartner et al., 1997; Wagner et al., 2001; Muscheler et al., 2004; Adolphi et al., 2014) and GISP2 (Finkel and Nishiizumi, 1997) ice cores. It also includes ^{10}Be data from the NGRIP, EDML, EDC, and Vostok ice cores around the Laschamp geomagnetic excursion (Raisbeck et al., 2017). It has been extended to the present using the ^{10}Be stack of Muscheler et al. (2016). This 70,000-year ^{10}Be stack provides relative changes of ^{14}C production rates under the assumption that ^{14}C and ^{10}Be production rates are directly proportional, as indicated by the most recent production rate models (e.g., Herbst et al., 2017).

For paleointensity-based estimates, we employ (1) the North Atlantic Paleointensity Stack, or NAPIS, by Laj et al. (2000) as extended by Laj et al. (2002), (2) the Global Paleointensity Stack, or GLOPIS, by Laj et al. (2004), (3)

https://doi.org/10.5194/cp-2019-159
Preprint. Discussion started: 14 January 2020

Climate of the Past
Discussions

a high-resolution paleointensity stack from the Black Sea (Nowaczyk et al., 2013), and (4) a paleointensity stack from Iberian Margin sediments (Channell et al., 2018). In principle, stacks of widely distributed cores (NAPIS/GLOPIS) are expected to yield a better representation of the global geomagnetic dipole moment, whereas the paleointensity stacks from the Black Sea and the Iberian Margin avoid some of the problems associated with coring disturbances. The four different paleointensity stacks were converted to ^{14}C production rates using the production rate model of Herbst et al. (2017), the local interstellar spectrum of Potgieter et al. (2014), and assuming a constant solar modulation potential of 630 MeV.

An alternative approach to estimating the ^{14}C production rate is to combine an atmospheric radiocarbon budget with a prognostic carbon cycle model. Here simulations are performed with the Bern3D model and forced by reconstructed changes in atmospheric $\Delta^{14}C$ and CO_2 over the last 50 kyr. Both the IntCal13 calibration curve (Reimer et al., 2013) and the Hulu Cave $\Delta^{14}C$ dataset (Cheng et al., 2018) are used. The ^{14}C production rate Q is calculated, each model year, from the air-sea $^{14}CO_2$ flux (F_{as}), the atmosphere-land $^{14}CO_2$ flux (F_{ab}), the loss of ^{14}C due to radioactive decay, and the change ($\dot{I}_a$) in the atmospheric ^{14}C inventory (I_a):

$$Q = F_{as} + F_{ab} + \lambda I_a + \dot{I}_a \tag{2}$$

where λ is the radioactive decay constant for ^{14}C, i.e., $\lambda = \ln 2/5700$ years = 1.2160×10^{-4} yr^{-1}. The radioactive decay term λI_a and the change in inventory $\dot{I}_a$ follow the reconstructed $\Delta^{14}C$ and CO_2 records, whereas F_{as} and F_{ab} are explicitly computed by the model. The F_{as} term depends strongly on the carbon cycle scenario under consideration (see Sect. 2.4 and Table 1). For comparison with other reconstructions, Q is converted into a relative value by normalizing it by the preindustrial value.

3 Results and discussion

3.1 $\Delta^{14}C$ response to step changes

We use step changes in the ^{14}C production rate, and in selected carbon cycle parameters, to gain insight into the characteristic magnitude and time scale of the corresponding $\Delta^{14}C$ changes (Fig. 4). Besides variations of the production rate, changes in ocean circulation and air-sea gas exchange are considered the most important factors affecting atmospheric $\Delta^{14}C$. Their effect on $\Delta^{14}C$ can be understood in terms of their effect on the reservoir sizes involved in the global carbon cycle and on the exchange rates between the reservoirs. We investigate the relative importance of the major global carbon reservoirs (atmosphere, terrestrial biosphere, ocean, and sediments) by considering four different model configurations (see Sect. 2.3), with particular emphasis on the role of marine sediments.

https://doi.org/10.5194/cp-2019-159
Preprint. Discussion started: 14 January 2020

Climate of the Past Discussions

In model studies, the process of sedimentation (here used specifically to refer to the balance between deposition and remineralization/dissolution at the sediment-water interface) is often neglected because it is a relatively minor flux. In the Bern3D model, sedimentation removes only about 0.46 Gt C and 45.31 mol ^{14}C per year in the preindustrial steady state. Indeed, interaction with the sediments has little influence on the global mean value of oceanic $\Delta^{14}C$, and therefore atmospheric $\Delta^{14}C$, as long as the total oceanic amount of carbon remains approximately constant (Siegenthaler et al., 1980); however, this is not always true, particularly in the case of millennial-scale climate perturbations. The differences between the two sets of model runs shown in Fig. 4 (i.e., ALL versus OCN-LND, and OCN-SED versus OCN) are due to sedimentation-driven changes in the ocean carbon inventory. In order to facilitate our discussion, we will only make direct comparisons between model runs ALL and OCN-LND. We note that the ^{14}C exchange rate between the atmosphere and the terrestrial biosphere is only of minor importance for long time scales of millennia and more.

3.1.1 Change of ^{14}C production

At steady state, the relative change of atmospheric $\Delta^{14}C$ is equal to the relative change of the ^{14}C production rate, irrespective of the individual reservoirs considered. Fig. 4 shows that atmospheric $\Delta^{14}C$ increases by about 100 permil (or 10 percent) when the production rate is increased by 10 percent. In model run ALL, $\Delta^{14}C$ increases approximately exponentially to its new steady-state value with a characteristic time constant T of about 6170 years (i.e., $1 - 1/e \approx$ 63 percent of the total change in $\Delta^{14}C$ occurs within 6170 years). This e-folding time scale is close to the mean lifetime of ^{14}C (~8223 years), which is modulated by the time required for equilibration between the atmosphere and the ocean (i.e., the time scale for deep ocean ventilation, of the order of hundreds to 1000 years). In the next section, we will investigate the effect of ocean carbon cycle processes on atmospheric $\Delta^{14}C$.

Note that for simplicity, we investigated only step changes in atmospheric production, although, in reality, ^{14}C production varies continuously over time due to changes in the solar and/or geomagnetic modulation of the cosmic radiation. This results in a non-steady state value of atmospheric $\Delta^{14}C$.

3.1.2 Change of ocean circulation

The exchange rate between the surface and deep ocean is mainly determined by physical transport and mixing processes. The overall effect of these processes is to transport ^{14}C-enriched surface waters to the thermocline and deep ocean, where waters are typically ^{14}C-depleted. In addition, the nutrient supply by transport and mixing plays an important role in determining the production and export of biogenic material from the surface ocean, constituting a second pathway for transporting ^{14}C to the deep ocean.

In the Bern3D model, the tunable model parameters affecting the ventilation of the deep ocean include a scale factor τ for the wind stress field and vertical diffusivity K_V. Fig. 4 shows the atmospheric $\Delta^{14}C$ response after a

https://doi.org/10.5194/cp-2019-159
Preprint. Discussion started: 14 January 2020

Climate of the Past
Discussions

sudden decrease of τ and K_V by 50 percent. Although a halving of τ and K_V does not represent a realistic change, the resulting state of the ocean's large-scale overturning circulation can be interpreted in terms of the "ideal age" of water, which represents the average time since a water mass last made surface boundary contact. The new steady-state ideal age after a halving of τ and K_V is almost three times greater than the preindustrial steady-state value (i.e., ~1664 years versus ~613 years). This "ageing" of the ocean is achieved through a weakening and shoaling of the global meridional overturning circulation as evident from a moderate reduction in the meridional overturning stream function for the Indo-Pacific Ocean from about 14 to 9.5 Sv (1 Sv = 10^6 m^3 s^{-1}), and a very strong reduction from about 18 to 8 Sv in the Atlantic meridional overturning stream function, consistent with evidence for the glacial ocean. Here, as expected, the overall effect of deep water ageing is a stronger vertical $\Delta^{14}C$ gradient in the water column and a subsequent increase in atmospheric $\Delta^{14}C$. The exact nature of the $\Delta^{14}C$ response, however, depends on the carbon reservoirs considered.

If sedimentation is neglected, the time required for $\Delta^{14}C$ to adjust to step changes in τ and K_V is relatively short. Atmospheric $\Delta^{14}C$ increases rapidly to its new steady-state value of ~159 permil, with a time constant T of about 600 years. This increase of $\Delta^{14}C$ can be explained by the fact that, owing to a weaker and shallower overturning circulation, a comparatively large amount of carbon is moved from the atmosphere to the ocean. More specifically, the atmospheric carbon inventory decreases by 14.6 percent, whereas the atmospheric ^{14}C inventory decreases by only 1.1 percent (Fig. 5c). The ^{14}C being produced in the atmosphere is therefore diluted by a smaller carbon inventory, increasing the atmospheric $^{14}C/C$ ratio; this asymmetry in the drawdown of CO_2 and $^{14}CO_2$ is what permits the increase of atmospheric $\Delta^{14}C$. Since the ocean carbon inventory changes by only +0.2 percent, the $\Delta^{14}C$ value for the global ocean is nearly unaffected, a decrease of only ~11 permil in the new steady state (Fig. 6g).

In the model run with sedimentation, there are two distinct time constants. A rapid increase of atmospheric $\Delta^{14}C$ occurs, ~143 permil in the first few hundred years, then $\Delta^{14}C$ gradually decreases to its final value of ~91 permil after tens of thousands of years. Reduced deep ocean ventilation is again responsible for the rapid $\Delta^{14}C$ change and the respective time constant (T = ~480 years). The second time constant of ~23,390 years is due to the relatively long time required for adjustment of the ocean carbon inventory to ocean circulation-driven changes in sedimentation.

The process of ocean circulation interacts with the efficiency of the ocean's biological carbon pump, via its impact on export production, ocean interior oxygen levels, and seawater carbonate chemistry/equilibria. This has important implications for the sedimentation of biogenic material at the sea floor and, on a time scale of tens of thousands of years, the total oceanic amount of carbon. Through this coupling of ocean circulation and sedimentation via the biological carbon pump, a halving of τ and K_V leads to a 9.8 percent increase of the ocean carbon inventory in the new steady state (Fig. 5e). Qualitatively, a reduction in the ocean's overturning circulation leads to a lower surface nutrient supply, which limits the production and export of biogenic material from the surface ocean. This, in turn, decreases the fluxes of POC and $CaCO_3$ to the sea floor, with major consequences for the magnitude of their sedimentation. At the same time, a constant amount of DIC, ALK, and nutrients is added to the ocean from terrestrial

https://doi.org/10.5194/cp-2019-159
Preprint. Discussion started: 14 January 2020

weathering which is no longer balanced by the sedimentation flux (this is what permits a larger ocean carbon inventory). The overall effect is a gradual reduction of global-ocean $\Delta^{14}C$ by ~76 permil (Fig. 6g), which dilutes the initial atmospheric $\Delta^{14}C$ peak by 52 permil.

3.1.3 Change of gas transfer velocity

It takes about a decade for the isotopic ratios of carbon to equilibrate between the atmosphere and a ~75-m thick surface mixed layer by air-sea gas exchange alone (Broecker and Peng, 1974). A consequence of this is that the surface ocean is undersaturated with respect to atmospheric $\Delta^{14}C$ (see Fig. 3). The choice of gas transfer velocity k_w as a function of wind speed is critical for the efficiency of air-sea gas exchange. A reduction of k_w corresponds to a higher resistance for gas transfer across the air-sea interface, which means that the ^{14}C produced in the atmosphere escapes into the surface ocean at a slower rate. The effect of a lower k_w is a larger air-sea gradient of $\Delta^{14}C$ and higher atmospheric $\Delta^{14}C$ values. In contrast, the $\Delta^{14}C$ value for the surface ocean is nearly unaffected so long as the ocean carbon inventory remains approximately constant, since the vertical gradient of $\Delta^{14}C$ in the ocean is dominated by physical transport and mixing processes. Although the exact nature of the gas transfer velocity under glacial climate conditions remains unclear, k_w represents a straightforward way to reduce the model's air-sea exchange efficiency due to theoretical changes in wind stress, sea ice, etc.

Fig. 4 shows how atmospheric $\Delta^{14}C$ responds to a perturbation in the gas transfer velocity. In the model run without sedimentation, reduction of k_w to 0 percent of its preindustrial value, in the model's north (> 60°N) and south (> 48°S) polar areas, leads to a moderate increase of atmospheric $\Delta^{14}C$ in the new steady state. The amplitude of $\Delta^{14}C$ change is ~42 permil, which is achieved with an e-folding time scale T of about 180 years. This relatively short time constant can be explained by the multidecadal time scale required for $\Delta^{14}C$ to equilibrate between the model's atmosphere, upper ocean, and terrestrial biosphere. As shown in Fig. 6, the global mean $\Delta^{14}C$ values for the surface, deep, and global ocean in the new steady state are only slightly different from the preindustrial steady-state values, as expected from the fact that the ocean carbon inventory remains relatively stable.

Interestingly, if sedimentation is included in the model, the final value of atmospheric $\Delta^{14}C$ is much higher (~91 permil). In this case, a perturbation in k_w leads to a very rapid initial increase of $\Delta^{14}C$ (~42 permil), and a much slower subsequent increase of $\Delta^{14}C$ (~49 permil). The latter has an e-folding time scale T of about 14,200 years. This slow doubling of the initial $\Delta^{14}C$ increase is unexpected, but can be explained by the fact that a reduction of k_w involves also a reduction of air-sea O_2 gas exchange in the deep water formation regions, decreasing the oceanic oxygen that is available for transport to the deep ocean. This, in turn, implies lower oxygen concentrations in the water column and the sediment pore waters, decreasing the rate of POC remineralization in the sediments. Reducing this has the overall effect of strengthening POC sedimentation at the sea floor, causing the ocean carbon inventory to decrease. As shown in Fig. 5, the total oceanic amount of carbon decreases by 5.9 percent in the new steady state, resulting in elevated $\Delta^{14}C$ values for the surface (+56 permil), deep (+30 permil), and global (+37 permil) ocean as well as for the

https://doi.org/10.5194/cp-2019-159
Preprint. Discussion started: 14 January 2020

Climate of the Past Discussions

atmosphere (+91 permil) (see Fig. 6). Note that the increase in atmospheric $\Delta^{14}C$ is not accompanied by a significant change in the atmospheric carbon (CO_2) inventory (i.e., it decreases by only 2.2 to 3.3 percent).

Overall, findings from these sensitivity experiments demonstrate that (1) the response of atmospheric $\Delta^{14}C$ to changes in the internal parameters of the ocean carbon cycle, in contrast to ^{14}C production changes, depends strongly on whether or not sedimentation at the sea floor is simulated, (2) the e-folding time scale for the initial adjustment of atmospheric $\Delta^{14}C$ to ocean carbon cycle changes, i.e., changes in ocean circulation and gas exchange, is shorter than that for production changes (i.e., ~600 years and ~180 years versus ~6170 years), (3) air-sea gas exchange, in contrast to ocean circulation, has only a small effect on atmospheric CO_2, and (4) on time scales of tens of thousands of years changes in the sedimentation of biogenic material can potentially diminish (or elevate) the atmospheric $\Delta^{14}C$ value. This is new, important information for future paleoclimate simulations, indicating that changes in $\Delta^{14}C$ may be overestimated (or underestimated) in models that do not simulate the interaction between sediments and the water column.

3.2 Role of ^{14}C production in past $\Delta^{14}C$ variability

We now consider the component of past atmospheric $\Delta^{14}C$ variability caused by production changes alone. Fig. 7 shows the results of model runs using different reconstructions of the ^{14}C production rate, as inferred from paleointensity data and from ice-core ^{10}Be fluxes. The global carbon cycle is assumed to be constant and under preindustrial conditions for these simulations (i.e., scenario MOD is used). Our analysis is restricted to the glacial portion of the record (50 to 18 kyr BP), in part because this is the time period which experiences the largest production changes, and in part because we did not attempt to reproduce the ~80 ppm change in atmospheric CO_2 that occurred during the last glacial termination. As we have already noted, much research over the last decades has attempted to explain the observed glacial-interglacial variations in atmospheric $\Delta^{14}C$ and CO_2, and this was not the goal of this study.

At first glance, the millennial-scale structure of model-simulated $\Delta^{14}C$ is comparable to that of the reconstructions. These similarities appear to be highest for the oldest portion of the record, roughly before 30 kyr BP. The model reproduces major features of the reconstructed $\Delta^{14}C$ variability such as the large changes associated with the Laschamp (~41 kyr BP) and Mono Lake (~34 kyr BP) geomagnetic excursions. These two events are clearly expressed as distinct maxima in all model-simulated records. A more detailed comparison reveals a high correlation between the modelled and reconstructed $\Delta^{14}C$ values between 50 and 33 kyr BP. Of note is the better agreement with the new Hulu Cave $\Delta^{14}C$ dataset as compared to the IntCal13 calibration curve (i.e., Pearson correlation coefficient r of 0.96 versus 0.91). This is likely due to the fact that the Laschamp excursion is smoothed/smeared out during the stacking process of the IntCal13 $\Delta^{14}C$ datasets (Adolphi et al., 2018). The correlation between modelled and reconstructed $\Delta^{14}C$ is much weaker during the millennia after the Mono Lake excursion (33 to 18 kyr BP; r = 0.52 to 0.64). While it is clear that much of the millennial-scale variation in $\Delta^{14}C$ is driven by past changes in ^{14}C production,

https://doi.org/10.5194/cp-2019-159
Preprint. Discussion started: 14 January 2020

the model fails to reproduce the glacial level of $\Delta^{14}C$ and also does not capture the ~15,000-year persistent elevation of $\Delta^{14}C$ or the subsequent decrease of $\Delta^{14}C$ after ~25 kyr BP.

The reconstructions suggest that the highest values of $\Delta^{14}C$ occurred during the Laschamp excursion, with a maximum value of ~595 permil at 41.1 kyr BP found in the IntCal13 record. The Hulu Cave record indicates even higher values for the Laschamp event ($\Delta^{14}C$ = ~742 permil, at 39.7 kyr BP). In contrast, the model is able to simulate maximum $\Delta^{14}C$ values of only ~364 permil at 40.4 kyr BP, and ~236 permil at 40.5 kyr BP, as predicted by the paleointensity-based and ice-core ^{10}Be-based production rate estimates, respectively. Although the model is unable to reproduce the reconstructed values of $\Delta^{14}C$, the modelled amplitude of the variation in $\Delta^{14}C$ in response to the Laschamp event shows a reasonable agreement with the reconstructed amplitude of $\Delta^{14}C$ change found in the IntCal13 record (~240 permil). The $\Delta^{14}C$ change predicted by paleointensity data has a maximal amplitude of about 320 permil, whereas the ice-core ^{10}Be data indicate a smaller amplitude (~224 permil). Note that the IntCal13 and model-simulated amplitudes of the Laschamp-related $\Delta^{14}C$ change are about two times smaller than that observed in the Hulu Cave record (~575 permil), which is more likely to be correct.

Moving onto the full glacial record (50 to 18 kyr BP), there are considerable discrepancies between reconstructed and modelled $\Delta^{14}C$ ($\Delta\Delta^{14}C$; see Fig. 7). The use of ice-core ^{10}Be data to predict past changes in $\Delta^{14}C$ results in the largest $\Delta\Delta^{14}C$, with offsets between the records as high as ~544 to 558 permil (root-mean-square error $RMSE$ = 404 to 408 permil). Model-simulated $\Delta^{14}C$ given by paleointensity data varies widely between the four available reconstructions, yielding $\Delta\Delta^{14}C$ values of ~325 to 639 permil ($RMSE$ = 206 to 455 permil). Note that the upper limit of the paleointensity-based $\Delta\Delta^{14}C$ overlaps with the ice-core ^{10}Be-based $\Delta\Delta^{14}C$. Given the uncertainties associated with the reconstruction of past changes in ^{14}C production, accurate predictions of its contribution to past changes in $\Delta^{14}C$ are challenging. Nonetheless, the substantial systematic offsets between the model-simulated and reconstructed $\Delta^{14}C$ records after ~33 kyr BP point toward insufficiently high ^{14}C production rates over this period of time. The question arises as to whether another factor besides geomagnetic modulation of the cosmic ray intensity was responsible for elevated glacial $\Delta^{14}C$ levels. The effect of ocean carbon cycle changes on the evolution of atmospheric $\Delta^{14}C$ is considered next.

3.3 Carbon cycle contribution to high glacial $\Delta^{14}C$ levels

Here we investigate the magnitude and timing of the maximum possible $\Delta^{14}C$ change during the last glacial period, obtained by running the Bern3D model with eight different carbon cycle scenarios (see Table 1). For the sake of clarity, we will discuss only the results of model runs using the mean paleointensity-based ^{14}C production rate, though all available reconstructions were used. We emphasize that this is not a best-guess estimate of paleointensity-based ^{14}C production. One should focus on the relative changes of $\Delta^{14}C$ between model scenarios, and how specific carbon cycle processes affect the glacial level of $\Delta^{14}C$.

https://doi.org/10.5194/cp-2019-159
Preprint. Discussion started: 14 January 2020

Modelled 50,000-year records of atmospheric $\Delta^{14}C$ and CO_2 plus corresponding reconstructed histories are shown in Fig. 8. In order to provide a basis for comparison of modelling efforts, the results of model run MOD (which assumes a constant preindustrial carbon cycle) are presented. The influence of ocean carbon cycle changes on atmospheric $\Delta^{14}C$ was tested in the other model runs. Interestingly, the forcing fields for model run PAL (orbital parameters, greenhouse gas radiative forcing, and ice sheet extent) have only a minimal impact on $\Delta^{14}C$. The PAL forcing fields also do not achieve sufficiently low glacial CO_2 concentrations. Only a slight reduction of atmospheric CO_2 by ~20 ppm could be achieved, which unrealistically occurs during the last glacial termination (CO_2 = 258.07 ppm, at 14.6 kyr BP). With hypothesized carbon cycle changes, the agreement between observed and modelled CO_2 during the last glacial period is good (as by design), but the deglacial CO_2 rise is lagged and ~60 ppm too small at 11 kyr BP. Since this study focuses on glacial $\Delta^{14}C$ levels before incipient deglaciation at ~18 kyr BP, we will not discuss the lag any further.

Running the model with additional carbon cycle changes leads to an improvement of modelled $\Delta^{14}C$ as compared to model run PAL. The amplitude of atmospheric $\Delta^{14}C$ change is highest for runs CIRC, VENT, and VENTx. This behavior is due to the fact that, owing to a reduction of τ, K_V, and k_w, strong vertical $\Delta^{14}C$ gradients in the ocean, as well as a large air-sea $\Delta^{14}C$ gradient, are established. As shown in Fig. 8, the reduction in ocean ventilation is clearly expressed in the observed increase of the model ocean's ideal age as well as surface- and deep-water reservoir ages, the latter two being equivalent to radiocarbon reservoir age offsets following Soulet et al. (2016). The deep-water reservoir age (i.e., B-Atm age offset) provides a measure of the radiocarbon disequilibrium between the deep ocean and the atmosphere, which arises due to the combined effect of air-sea gas exchange efficiency and the strength of the ocean's overturning circulation (i.e., the deep ocean ventilation rate). As a consequence of the reduction in the meridional overturning circulation, model run CIRC predicts a substantial increase in B-Atm for the glacial ocean, with values reaching as high as ~3236 ^{14}C years, nearly double the preindustrial value of ~1626 ^{14}C years. Model run VENT predicts a slightly larger increase (+166 ^{14}C years) in the glacial ocean's B-Atm, due to the inhibition of air-sea gas exchange. The "oldest" waters are found in run VENTx where air-sea gas exchange is severely restricted, giving a glacial B-Atm value of ~3576 ^{14}C years. This would imply that the model's glacial ocean was more than two times older than its preindustrial counterpart. Further support comes from the model-simulated ideal age, which indicates that the ventilation time scale for the glacial ocean was about two times longer than for the preindustrial ocean (i.e., ~1297 years versus ~613 years).

Indirect evidence for deep water ageing can be provided by the occurrence of depleted ocean interior oxygen levels, due to the progressive consumption of dissolved oxygen during POC remineralization. This situation would signal higher values of apparent oxygen utilization (AOU = $O_{2,pre} - O_2$). Model runs CIRC, VENT, and VENTx do indeed indicate a large increase in AOU of about 95 mmol m^{-3} from its preindustrial value of ~150 mmol m^{-3}. The reason for this AOU increase is that a reduction of deep ocean ventilation permits enhanced accumulation of remineralized carbon in the ocean interior and therefore a more efficient biological carbon pump. Model runs BIO, PHYS-BIO, and PHYS-BIOx allow us to investigate the impact of other biological carbon pump changes on

https://doi.org/10.5194/cp-2019-159
Preprint. Discussion started: 14 January 2020

atmospheric $\Delta^{14}C$ and CO_2 (i.e., changes in the $CaCO_3$-to-POC export ratio and POC remineralization length scale). While these changes lead to an effective atmospheric CO_2 drawdown mechanism, model results confirm that their effect on atmospheric $\Delta^{14}C$ is much less important (see Fig. 8).

Model run VENTx gives the best results with respect to glacial levels of $\Delta^{14}C$, with a maximum underestimation of ~202 to 229 permil ($RMSE$ = 103 to 110 permil) and a relatively good correlation (r = 0.79 to 0.91). Only one model parameter was changed for run VENTx as compared to runs CIRC and VENT, namely, the polar gas transfer velocity k_w was reduced to 0 percent of its preindustrial value during the last glacial. In this extreme scenario, we assume that sea ice cover extended in the northern hemisphere as far south as 60°N and in the southern hemisphere as far north as 48°S, which is not supported by the reconstructions (Gersonde et al., 2005; Allen et al., 2011). Nonetheless, considering extreme assumptions about polar air-sea exchange efficiency under glacial climate conditions is interesting for two reasons: (1) a change in gas exchange hardly affects the atmospheric CO_2 concentration, and (2) an additional change of atmospheric $\Delta^{14}C$ could be achieved on a time scale of tens of thousands of years through a change in sedimentation at the sea floor. This behavior has important implications for the glacial atmosphere, which is characterized by high $\Delta^{14}C$ levels in conjunction with low but relatively stable CO_2 concentrations. In contrast to a change in ocean circulation, air-sea gas exchange is a dedicated $\Delta^{14}C$ control knob that can be invoked for a further increase of atmospheric $\Delta^{14}C$ without changing atmospheric CO_2. Here, an additional increase of $\Delta^{14}C$ by ~130 permil, as compared to runs CIRC and VENT, is achieved if gas exchange is reduced permanently to 0 percent in the polar regions.

While the modelled $\Delta^{14}C$ values for run VENTx show rather good agreement with the reconstructions between 50 and 33 kyr BP (r = 0.92 to 0.96; $RMSE$ = 74 to 102 permil), considerable discrepancies remain for the younger portion of the record. The analysis shown in Fig. 9 illustrates that even with extreme changes in the ocean carbon cycle it is very difficult to reproduce the reconstructed $\Delta^{14}C$ values after ~33 kyr BP. During this period of time, model run VENTx underestimates $\Delta^{14}C$ by up to ~203 permil ($RMSE$ = 118 to 128 permil), and is very poorly (r = 0.1) correlated with the reconstructions, confirming that there are still considerable gaps in our understanding. Although it may be possible that permanent North Atlantic-Arctic and Antarctic sea ice cover extended to lower and higher latitudes than previously reconstructed, we conclude from our model study that even extreme assumptions about sea ice cover are insufficient to explain the elevated $\Delta^{14}C$ levels after ~33 kyr BP. It appears instead that the glacial ^{14}C production rate was higher than previously estimated and/or the reconstruction of glacial atmospheric $\Delta^{14}C$ levels is biased high. The older portion of the $\Delta^{14}C$ record is based on data from archives other than tree rings (i.e., plant macrofossils, speleothems, corals, and foraminifera) (Reimer et al., 2013), providing, except for the Lake Suigetsu plant macrofossil data (Bronk Ramsey et al., 2012), only indirect measurements of atmospheric $\Delta^{14}C$. Note that these data show uncertainty in calendar age that propagate into the estimation of past atmospheric $\Delta^{14}C$ levels.

Large uncertainties in the pre-Holocene ^{14}C production rate also hamper our qualitative and quantitative interpretation of the atmospheric $\Delta^{14}C$ record. There is considerable disagreement between the available

https://doi.org/10.5194/cp-2019-159
Preprint. Discussion started: 14 January 2020

reconstructions of past changes in ^{14}C production (Fig. 1). Paleointensity-based estimates typically predict higher ^{14}C production rates than ice-core ^{10}Be-based ones. An exception is the paleointensity stack from Channell et al. (2018), which predicts lower production rates. But, irrespective of the scatter, it is clear that all of the ^{14}C production rate estimates are insufficiently high to explain the elevated $\Delta^{14}C$ levels during the last glacial. Given the uncertainties in these estimates, it is very difficult to quantitatively describe the role of the ocean carbon cycle in determining the $\Delta^{14}C$ and CO_2 levels in the glacial atmosphere.

3.4 Reconstructing the ^{14}C production rate by deconvolving the $\Delta^{14}C$ record

The unresolved discrepancy between reconstructed and model-simulated $\Delta^{14}C$ raises the question how the ^{14}C production rate would have had to evolve to be consistent with the IntCal13 calibration curve or the new Hulu Cave $\Delta^{14}C$ dataset. This question is addressed by deconvolving the atmospheric $\Delta^{14}C$ reconstruction over the last 50 kyr, using the Bern3D carbon cycle model forced with reconstructed atmospheric histories of $\Delta^{14}C$ and CO_2 (see Eq. [2]). The carbon cycle scenarios described in Table 1, with the exception of MOD, are used in order to provide an estimate of the uncertainty associated with the model's glacial ocean carbon cycle. We note that the carbon cycle scenarios are not designed to capture the specific features of the last glacial termination, and therefore the results of the deconvolution over this time period must be considered very preliminary (and viewed tentatively). A detailed analysis of the Holocene ^{14}C production rate is available in the literature (Roth and Joos, 2013). Finally, we consider the uncertainties associated with the older portion of the $\Delta^{14}C$ record by deconvolving both the IntCal13 and Hulu Cave $\Delta^{14}C$ records. Hulu Cave data overlap with IntCal13 between ~10.6 and 33.3 kyr BP (Cheng et al., 2018), as expected from the fact that IntCal13 between 10.6 and 26.8 kyr BP is based in part on Hulu Cave stalagmite H82 (Southon et al., 2012), whereas there are substantial offsets before ~30 kyr BP.

Fig. 10 shows the new, model-based reconstruction of past changes in ^{14}C production. Before the onset of the Laschamp excursion at ~42 kyr BP, production rates as inferred from the Hulu Cave record are near modern levels, whereas those obtained from the IntCal13 record are somewhat higher than modern. As expected, peak production occurs during the Laschamp event (~42 to 40 kyr BP), with the Hulu Cave dataset yielding the largest amplitude (factor of ~2 greater than modern). The IntCal13 record predicts a smaller amplitude of ~1.6 times the modern value. Both $\Delta^{14}C$ records predict production minima at ~37 kyr BP (~7 percent higher than modern) and ~32 kyr BP (~5 percent higher than modern), interrupted by a prominent peak (factors of ~1.5 and ~1.4, respectively) during the Mono Lake geomagnetic excursion (~34 kyr BP), though the details of the timing and structure differ between the two records. Between 32 and 22 kyr BP, model-based estimates of the ^{14}C production rate are ~1.3 times the modern value, which then decrease to around modern levels by HS1 (~18 kyr BP).

Model-based estimates of ^{14}C production during the last glacial are typically higher than paleointensity-based and ice-core ^{10}Be-based ones, as expected from the analysis in Sect. 3.2. Between 32 and 22 kyr BP, the deconvolutions of the IntCal13 and Hulu Cave $\Delta^{14}C$ records give estimates that are about 17.5 percent higher than the reconstructions.

https://doi.org/10.5194/cp-2019-159
Preprint. Discussion started: 14 January 2020

It is important to note that the differences between the production rate estimates inferred from the proxy data (i.e., paleointensity data and ice-core ^{10}Be fluxes) are as large as the differences between our deconvolution results and the reconstructions (see Table 2). As shown in Fig. 11, it is extremely difficult to reconcile the discrepancies between reconstructed and model-based ^{14}C production on the basis of carbon cycle changes alone. Nonetheless, the fact remains that two independent estimates of the ^{14}C production rate (estimates inferred from paleointensity data and from ice-core ^{10}Be fluxes) show systematically lower rates than those obtained by our model-based deconvolution of atmospheric Δ^{14}C. The differences between the results shown in Fig. 10 and Fig. 11 and Table 2 stem from various uncertainties that are discussed next.

Uncertainties associated with the glacial ocean carbon cycle (Fig. 10, colored shading; Fig. 11, colored lines) are systematic in our approach. The deconvolutions, e.g., of the Hulu Cave Δ^{14}C record, under different model scenarios are offset against one another, whereas the millennial-scale variability is maintained (see Fig. 11). We do not attempt to resolve uncertainties associated with Dansgaard-Oeschger warming events and related Antarctic and tropical climatic excursions in the model runs. Such climatic events may have influenced the atmospheric radiocarbon budget, but their influence on long-term variations in atmospheric Δ^{14}C, and therefore inferred production rates, is presumably limited. As may be expected, the lowest production rates (the lowest F_{as} values) are found in extreme scenario VENTx and the highest in scenarios PAL and BIO, mirroring the high and low glacial Δ^{14}C levels achieved by these model scenarios as discussed in Sect. 3.3. Note that there is a large uncertainty in the model-based ^{14}C production rate stemming from uncertainties associated with the reconstruction of past changes in atmospheric Δ^{14}C, in particular the older portion of the Δ^{14}C record.

A shortcoming of paleointensity-based reconstructions of the ^{14}C production rate is that they neglect changes in the solar modulation of the cosmic radiation. The solar modulation potential, which describes the impact of the solar magnetic field on isotope production, varied between 100 and 1200 MeV during the Holocene on decadal to centennial time scales, with a median value of approximately 565 MeV (Roth and Joos, 2013). A halving of the solar modulation potential (e.g., from 600 to 300 MeV) increases the ^{14}C production rate by about 25 percent for the modern geomagnetic field strength (Roth and Joos, 2013; see their Fig. 13). This sensitivity remains similar when changes in the strength of the geomagnetic field are limited as during the last ~35 kyr (Muscheler and Heikkilä, 2011). A shift to lower solar modulation potential could have materialized if the sun spent on average more time in the postulated "Grand Minimum" mode (Usoskin et al., 2014) during the last glacial than during the Holocene. The sensitivity of isotope production to variations in solar modulation potential becomes large during the Laschamp event when the intensity of the geomagnetic field was close to zero and changes in the solar modulation of the cosmic ray flux may have a discernible impact on the high Δ^{14}C levels found over this period. A reduction of the solar modulation potential from 600 to 0 MeV would double ^{14}C production during times of zero geomagnetic field strength (Masarik and Beer, 2009). However, it is likely that changes in the solar modulation potential were insufficient to explain the discrepancy between paleointensity-based production rate estimates and the results of our deconvolution, in particular for the post-Laschamp period and for the reconstruction by Channell et al. (2018). Uncertainties associated with the paleointensity-based reconstructions stem also from uncertainties in estimating the age-scales of the marine sediments and the geomagnetic field data.

The ice-core ^{10}Be-based reconstruction of past changes in ^{14}C production reflects, by definition, the combined influence of changes in the solar and geomagnetic modulation of the cosmic ray flux reaching the Earth. This method, therefore, avoids a fundamental shortcoming of reconstructions based on geomagnetic field data. The assumption is that the ^{10}Be and ^{36}Cl deposited on polar ice and measured in ice cores scales with the amount of cosmogenic isotopes in the atmosphere. A difficulty is to extrapolate measurements from a single or a few locations to the global atmosphere. Changes in climate influence atmospheric transport and deposition of ^{10}Be as well as the snow accumulation rate, which affect the ice-core ^{10}Be concentration (Elsässer et al., 2015). Furthermore, the sensitivity of ^{10}Be in polar ice versus the sensitivity of total production to magnetic field variations, or "polar bias", is a point of debate, but atmospheric transport models (Heikkilae et al., 2009; Field et al., 2006) and data analyses (Bard et al., 1997; Adolphi and Muscheler, 2016; Adolphi et al., 2018) reach different conclusions about its existence and magnitude. If a polar bias was present, it would lead to an underestimation of the geomagnetic modulation of the ice-core ^{10}Be flux and therefore the ^{14}C production rate.

Given the uncertainties associated with the proxy records, it may not be surprising that estimates of the ^{14}C production rate for the last 50 kyr, as obtained by three fundamentally different methods (geomagnetic field data from marine sediments, ^{10}Be and ^{36}Cl measurements in polar ice cores, and model-based deconvolution of atmospheric Δ^{14}C), disagree with one another, typically by order 10 percent and sometimes by up to 100 percent. At the same time, it is intriguing that two independent estimates of the ^{14}C production rate (i.e., estimates inferred from paleointensity and ice-core ^{10}Be data) give values that are systematically lower than what is required to match the Δ^{14}C reconstruction.

4 Summary and conclusions

It is generally assumed that atmospheric Δ^{14}C is controlled by abiotic processes such as atmospheric ^{14}C production, air-sea gas exchange, and ocean circulation and mixing. Here, results from sensitivity experiments with the Bern3D earth system model of intermediate complexity suggest that atmospheric Δ^{14}C is potentially quite sensitive to the interaction between sediments and the water column on multimillennial timescales. This rather surprising result is due to the coupling of ocean circulation and biogenic particle sedimentation via the biological carbon pump, which has important implications for the ocean carbon inventory. If the model's ocean carbon cycle is sufficiently perturbed, e.g., by changing the inputs or parameters controlling ocean circulation and/or gas exchange, the resulting shift in sedimentation has a significant impact on the total oceanic amount of carbon and therefore the average Δ^{14}C value of the ocean. On time scales of tens of thousands of years the impact of these changes on atmospheric Δ^{14}C is significant because of the long time scale associated with changes in the sedimentation of biogenic material. This is important information for long-term climate studies and paleoclimate modelling efforts concerning Δ^{14}C. Note that the representation of ocean-sediment interactions in the Bern3D is necessarily simplified compared to reality.

https://doi.org/10.5194/cp-2019-159
Preprint. Discussion started: 14 January 2020

Climate of the Past Discussions

Nonetheless, a change in the ocean carbon inventory linked with changing sedimentation should be discussed as one of the potentially important factors affecting atmospheric $\Delta^{14}C$ during the last glacial period.

The reason for the high $\Delta^{14}C$ values exhibited by the glacial atmosphere is still not clear. In order to investigate potential mechanisms governing glacial $\Delta^{14}C$ levels, the Bern3D model is again used as a tool. Results of model simulations forced only by production changes point out that none of the available reconstructions of the ^{14}C production rate can explain the full amplitude of $\Delta^{14}C$ change during the last glacial. In order to test the sensitivity of the model results with respect to the ocean carbon cycle state, various model parameters, i.e., different sets of physical and biogeochemical parameters, were "tuned" to match the glacial CO_2 level. From this, we find that atmospheric $\Delta^{14}C$ is most sensitive to changes in physical model parameters, in particular those controlling ocean circulation and gas exchange. In order to achieve an atmospheric $\Delta^{14}C$ value close to the glacial level, the gas transfer velocity in the polar regions had to be reduced by 100 percent. If interpreted as being due to a greater extent of permanent sea ice cover, a reduction in polar air-sea exchange efficiency is a possible explanation for high glacial $\Delta^{14}C$ levels. Although this hypothesis is compelling, such a scenario is not supported by the proxy records of Antarctic sea ice cover (Gersonde et al., 2005; Allen et al., 2011) and the $^{13}C/^{12}C$ ratio of atmospheric CO_2 (Eggleston et al., 2016).

Before model-simulated $\Delta^{14}C$ can be taken seriously, it must be demonstrated that the reconstruction of past changes in ^{14}C production is reliable. There is, however, a substantial amount of scatter in the paleointensity-based and ice-core ^{10}Be-based estimates of ^{14}C production. Here we adopt an alternative approach to estimating the ^{14}C production rate, which would indeed benefit from further constraints and lines of supporting evidence. Our deconvolution-based approach assumes that the ^{14}C production rate can be derived from an atmospheric radiocarbon budget, constructed using a prognostic carbon cycle model combined with the atmospheric $\Delta^{14}C$ record. Our model results suggest that the glacial ^{14}C production rate as inferred from paleointensity data and ice-core ^{10}Be fluxes may be underestimated by about 15 percent between 32 and 22 kyr BP. Note that our model-based estimates are associated with uncertainties arising from the reconstruction of the older portion of the $\Delta^{14}C$ record and the model simulation of the glacial ocean carbon cycle (e.g., a too high glacial air-sea CO_2 flux). Future improvements in the reconstruction of past changes in ^{14}C production and atmospheric $\Delta^{14}C$ would open up the possibility of attributing model deficiencies to real changes in the ocean carbon cycle. Ultimately, an improved knowledge of ^{14}C production during the last glacial, as well as more robust constraints on the prevailing climate conditions (e.g., ocean circulation, sea ice cover, and wind speed), are necessary to elucidate the processes permitting mysteriously high $\Delta^{14}C$ levels in the glacial atmosphere.

Appendix A: Complete description of the Bern3D model

The physical core of the Bern3D model is based on the 3-D rigid-lid ocean model of Edwards et al. (1998) as updated by Edwards and Marsh (2005). The forcing fields for the model integration are monthly mean wind stress data taken from NCEP/NCAR (Kalnay et al., 1996). Diapycnal mixing is parameterized with a uniform vertical diffusivity K_V of 2 x 10^{-5} m s^{-1}. The parameterization of eddy-induced transport is separated from that of isopycnal mixing, using the

https://doi.org/10.5194/cp-2019-159
Preprint. Discussion started: 14 January 2020

Gent-McWilliams skew flux (Griffies, 1998). Running at the same temporal and horizontal resolution, the one-layer energy-moisture balance atmosphere model performs an analysis of the energy budget of the Earth by involving solar radiation, infrared fluxes, evaporation and precipitation, and sensible and latent heat. The zonally averaged surface albedo climatology is taken from Kukla and Robinson (1980). Transport of moisture is performed by diffusion and advection and heat by eddy diffusion.

The Bern3D ocean carbon cycle model is based on the Ocean Carbon-Cycle Model Intercomparison Project (OCMIP-2) protocols. Air-sea gas exchange is parameterized using the standard gas transfer formulation adopted for OCMIP-2, except that the gas transfer velocity k_w parameterization is a linear function of wind speed (Krakauer et al., 2006) to which we have added a scale factor of 0.81 to match the observed global ocean inventory of bomb ^{14}C (Müller et al., 2008). It is assumed that CO_2 and O_2 are well-mixed in the atmosphere. Surface boundary conditions also include a virtual-flux term for biogeochemical tracers (e.g., DIC and ALK) to account for their dilution or concentration due to implicit freshwater fluxes. Modifications from the original OCMIP-2 biotic protocol include the prognostic formulation of new/export production as a function of light, temperature, and limiting nutrient concentrations, where the nutrient uptake follows Michaelis-Menten kinetics. The production of biogenic $CaCO_3$ and opal is computed on the basis of the modelled particulate organic carbon (POC) production and availability of silicate, with a maximum possible fraction of $CaCO_3$ material that can be produced. This threshold value is represented by the $CaCO_3$-to-POC export ratio. In the preindustrial control run, the global mean export ratio rr is 0.082.

Biogenic material that has been produced in the 75-m production zone is redistributed over the water column in order to parameterize the downward particle flux through the water column. A power-law model referred to as the Martin curve is used to describe the vertical POC flux profile, whereas both $CaCO_3$ and opal export are redistributed over the water column with an exponential curve. POC is remineralized instantaneously back to dissolved form according to Redfield stoichiometry and with a 250–m length scale l_{POC} (i.e., in 250 m, the POC flux declines by $1 - 1/e \approx 63$ percent). Likewise, $CaCO_3$ and opal are dissolved within one time step, with e-folding depths of 5066 and 10,000 m, respectively. Biogenic material reaching the model's sea floor forms the upper boundary condition of the 10-layer sediment model after Heinze et al. (1999) and Gehlen et al. (2006). The sediment model includes four solid sediment components (POC, $CaCO_3$, opal, and clay) and is based on the sediment advection and accumulation scheme as in the work of Archer et al. (1993). The rate of POC remineralization in the sediments is primarily determined by the pore water concentration of oxygen, whereas the sediment mineral dissolution rate is governed by the saturation state of pore waters with respect to $CaCO_3$ or opal. The weathering input of DIC, ALK, and nutrients into the ocean is added as a constant increment to each wet grid cell along the coastlines. Any material input from terrestrial weathering is considered "radiocarbon dead". The values for these fluxes were chosen so that at the end of the preindustrial spin-up, input (weathering) and output (sedimentation) are balanced. Additional details concerning the sediment model are provided in Tschumi et al. (2011) and the appendix of Jeltsch-Thömmes et al. (2019).

https://doi.org/10.5194/cp-2019-159
Preprint. Discussion started: 14 January 2020

The exchange of any isotopic perturbation between the atmosphere and the terrestrial biosphere is simulated by use of the four-box model of Siegenthaler and Oeschger (1987). The terrestrial biosphere is represented by four well-mixed compartments (ground vegetation plus leaves, wood, detritus, and soils), with a fixed total carbon inventory of 2220 Gt C. Net primary production is balanced by respiration of detritus and soils, and is set to 60 Gt C per year.

Data availability. All data generated or analyzed during this study can be made available upon request to the corresponding author (A.D.).

Author contribution. This study was designed by F.J. and A.D. with input from F.A. A.D. developed and performed the model simulations. F.A. provided production data. A.D. wrote the manuscript with contributions from the co-authors.

Competing interests. The authors declare that they have no conflict of interest.

Acknowledgements. This work was made possible by the Swiss National Science Foundation (#200020_172476) and by the UniBE international 2021 fellowship program of the U. Bern. F.A. was supported by the Swedish Research Council (Vetenskaprådet DNR: 2016-00218).

References

Adolphi, F., and Muscheler, R.: Synchronizing the Greenland ice core and radiocarbon timescales over the Holocene – Bayesian wiggle-matching of cosmogenic radionuclide records, Climate of the Past, 12, 15–30, 2016.

Adolphi, F., Muscheler, R., Svensson, A., Aldahan, A., Possnert, G., Beer, J., . . . Thiéblemont, R.: Persistent link between solar activity and Greenland climate during the Last Glacial Maximum, Nature Geoscience, 7, 662–666, 2014.

Adolphi, F., Ramsey, C. B., Erhardt, T., Edwards, R. L., Cheng, H., Turney, C. S., . . . Muscheler, R.: Connecting the Greenland ice-core and U/Th timescales via cosmogenic radionuclides: testing the synchroneity of Dansgaard–Oeschger events, Climate of the Past, 14, 1755–1781, 2018.

Allen, C. S., Pike, J., and Pudsey, C. J.: Last glacial–interglacial sea-ice cover in the SW Atlantic and its potential role in global deglaciation, Quaternary Science Reviews, 30, 2446–2458, 2011.

Archer, D., and Maier-Reimer, E.: Effect of deep-sea sedimentary calcite preservation on atmospheric CO_2 concentration, Nature, 367, 260–263, 1994.

Archer, D., Lyle, M., Rodgers, K., and Froelich, P.: What controls opal preservation in tropical deep-sea sediments?, Paleoceanography, 8, 7–21, 1993.

Archer, D., Winguth, A., Lea, D., and Mahowald, N.: What caused the glacial/interglacial atmospheric pCO_2 cycles?, Reviews of Geophysics, 38, 159–189, 2000.

https://doi.org/10.5194/cp-2019-159
Preprint. Discussion started: 14 January 2020

Audi, G., Bersillon, O., Blachot, J., and Wapstra, A. H.: The Nubase evaluation of nuclear and decay properties, Nuclear Physics A, 729, 3–128, 2003.

Bard, E., Raisbeck, G. M., Yiou, F., and Jouzel, J.: Solar modulation of cosmogenic nuclide production over the last millennium: comparison between ^{14}C and ^{10}Be records, Earth and Planetary Science Letters, 150, 453–462, 1997.

Baumgartner, S., Beer, J., Wagner, G., Kubik, P., Suter, M., Raisbeck, G. M., and Yiou, F.: ^{10}Be and dust, Nuclear Instruments and Methods in Physics Research Section B: Beam Interactions with Materials and Atoms, 123, 296–301, 1997.

Baumgartner, S., Beer, J., Masarik, J., Wagner, G., Meynadier, L., and Synal, H.-A.: Geomagnetic Modulation of the ^{36}Cl Flux in the GRIP Ice Core, Greenland, Science, 279, 1330–1332, 1998.

Bé, M.-M., Chisté, V., Dulieu, C., Mougeot, X., Chechev, V., Kondev, F., . . . Wang, B.: Table of Radionuclides (Comments on evaluations), Monographie BIPM-5, 7, 2013.

Berger, A. L.: Long-term variations of daily insolation and Quaternary climatic changes, Journal of the Atmospheric Sciences, 35, 2362–2367, 1978.

Broecker, W., and Barker, S.: A 190‰ drop in atmosphere's $\Delta^{14}C$ during the "Mystery Interval" (17.5 to 14.5 kyr), Earth and Planetary Science Letters, 256, 90–99, 2007.

Broecker, W. S., and Peng, T.-H.: Gas exchange rates between air and sea, Tellus, 26, 21–35, 1974.

Bronk Ramsey, C., Staff, R. A., Bryant, C. L., Brock, F., Kitagawa, H., van der Plicht, J., Schlolaut, G., Marshall, M. H., Brauer, A., Lamb, H. F., Payne, R. L., Tarasov, P. E., Haraguchi, T., Gotanda, K., Yonenobu, H., Yokoyama, Y., Tada, R., and Nakagawa, T.: A complete terrestrial radiocarbon record for 11.2 to 52.8 kyr B.P., Science, 338, 370–374, 2012.

Brovkin, V., Ganopolski, A., Archer, D., and Munhoven, G.: Glacial CO_2 cycle as a succession of key physical and biogeochemical processes, Climate of the Past, 8, 251–264, 2012.

Channell, J. E., Hodell, D. A., Crowhurst, S. J., Skinner, L. C., and Muscheler, R.: Relative paleointensity (RPI) in the latest Pleistocene (10-45 ka) and implications for deglacial atmospheric radiocarbon, Quaternary Science Reviews, 191, 57–72, 2018.

Cheng, H., Edwards, R. L., Southon, J., Matsumoto, K., Feinberg, J. M., Sinha, A., . . . Ning, Y.: Atmospheric $^{14}C/^{12}C$ changes during the last glacial period from Hulu Cave, Science, 362, 1293–1297, 2018.

Delaygue, G., Stocker, T. F., Joos, F., and Plattner, G.-K.: Simulation of atmospheric radiocarbon during abrupt oceanic circulation changes: trying to reconcile models and reconstructions, Quaternary Science Reviews, 22, 1647–1658, 2003.

Edwards, N. R., and Marsh, R.: Uncertainties due to transport-parameter sensitivity in an efficient 3-D ocean-climate model, Climate Dynamics, 24, 415–433, 2005.

Edwards, N. R., Willmott, A. J., and Killworth, P. D.: On the Role of Topography and Wind Stress on the Stability of the Thermohaline Circulation, Journal of Physical Oceanography, 28, 756–778, 1998.

Eggleston, S., Schmitt, J., Bereiter, B., Schneider, R., and Fischer, H.: Evolution of the stable carbon isotope composition of atmospheric CO_2 over the last glacial cycle, Paleoceanography, 31, 434–452, 2016.

Elsässer, C., Wagenbach, D., Levin, I., Stanzick, A., Christl, M., Wallner, A., . . . Dibb, J.: Simulating ice core ^{10}Be on the glacial–interglacial timescale, Climate of the Past, 11, 115–133, 2015.

Field, C. V., Schmidt, G. A., Koch, D., and Salyk, C.: Modeling production and climate-related impacts on ^{10}Be concentration in ice cores, Journal of Geophysical Research: Atmospheres, 111, https://doi.org/10.1029/2005JD006410, 2006.

Finkel, R. C., and Nishiizumi, K.: Beryllium 10 concentrations in the Greenland Ice Sheet Project 2 ice core from 3-40 ka, Journal of Geophysical Research: Oceans, 102, 26699–26706, 1997.

Fischer, H., Schmitt, J., Lüthi, D., Stocker, T. F., Tschumi, T., Parekh, P., . . . Wolff, E.: The role of Southern Ocean processes in orbital and millennial CO_2 variations – A synthesis, Quaternary Science Reviews, 29, 193–205, 2010.

Ganopolski, A., and Brovkin, V.: Simulation of climate, ice sheets and CO_2 evolution during the last four glacial cycles with an Earth system model of intermediate complexity, Climate of the Past, 13, 1695–1716, 2017.

Gehlen, M., Bopp, L. E., Aumont, O., Heinze, C., and Ragueneau, O.: Reconciling surface ocean productivity, export fluxes and sediment composition in a global biogeochemical ocean model, Biogeosciences, 3, 521–537, 2006.

Gersonde, R., Crosta, X., Abelmann, A., and Armand, L.: Sea-surface temperature and sea ice distribution of the Southern Ocean at the EPILOG Last Glacial Maximum—a circum-Antarctic view based on siliceous microfossil records, Quaternary Science Reviews, 24, 869–896, 2005.

Gkinis, V., Simonsen, S. B., Buchardt, S. L., White, J. W., and Vinther, B. M.: Water isotope diffusion rates from the NorthGRIP ice core for the last 16,000 years – Glaciological and paleoclimatic implications, Earth and Planetary Science Letters, 405, 132–141, 2014.

Griffies, S. M.: The Gent-McWilliams Skew Flux, Journal of Physical Oceanography, 28, 831–841, 1998.

Hain, M. P., Sigman, D. M., and Haug, G. H.: Distinct roles of the Southern Ocean and North Atlantic in the deglacial atmospheric radiocarbon decline, Earth and Planetary Science Letters, 394, 198–208, 2014.

Heikkilä, U., Beer, J., and Feichter, J.: Meridional transport and deposition of atmospheric ^{10}Be, Atmospheric Chemistry and Physics, 9, 515–527, 2009.

Heikkilä, U., Phipps, S. J., and Smith, A. M.: ^{10}Be in late deglacial climate simulated by ECHAM5-HAM – Part 1: Climatological influences on ^{10}Be deposition, Climate of the Past, 9, 2641–2649, 2013.

Heinze, C., Maier-Reimer, E., Winguth, A. M., and Archer, D.: A global oceanic sediment model for long-term climate studies, Global Biogeochemical Cycles, 13, 221–250, 1999.

Herbst, K., Muscheler, R., and Heber, B.: The new local interstellar spectra and their influence on the production rates of the cosmogenic radionuclides ^{10}Be and ^{14}C, Journal of Geophysical Research: Space Physics, 122, 23–34, 2017.

Hoff, U., Rasmussen, T. L., Stein, R., Ezat, M. M., and Fahl, K.: Sea ice and millennial-scale climate variability in the Nordic seas 90 kyr ago to present, Nature Communications, 7, doi:10.1038/ncomms12247, 2016.

Hughen, K., Lehman, S., Southon, J., Overpeck, J., Marchal, O., Herring, C., and Turnbull, J.: ^{14}C Activity and Global Carbon Cycle Changes over the Past 50,000 Years, Science, 303, 202–207, 2004.

https://doi.org/10.5194/cp-2019-159
Preprint. Discussion started: 14 January 2020

Climate of the Past Discussions

Huiskamp, W. N., and Meissner, K. J.: Oceanic carbon and water masses during the Mystery Interval: A model-data comparison study, Paleoceanography and Paleoclimatology, 27, https://doi.org/10.1029/2012PA002368, 2012.

Jeltsch-Thömmes, A., Battaglia, G., Cartapanis, O., Jaccard, S. L., and Joos, F.: Low terrestrial carbon storage at the Last Glacial Maximum: constraints from multi-proxy data, Climate of the Past, 15, 849–879, 2019.

Köhler, P., Muscheler, R., and Fischer, H.: A model-based interpretation of low-frequency changes in the carbon cycle during the last 120,000 years and its implications for the reconstruction of atmospheric $\Delta^{14}C$, Geochemistry Geophysics Geosystems, 7, 1–22, 2006.

Köhler, P., Nehrbass-Ahles, C., Schmitt, J., Stocker, T. F., and Fischer, H.: A 156 kyr smoothed history of the atmospheric greenhouse gases CO_2, CH_4, and N_2O and their radiative forcing, Earth System Science Data, 9, 363–387, 2017.

Kalnay, E., Kanamitsu, M., Kistler, R., Collins, W., Deaven, D., Gandin, L., . . . Joseph, D.: The NCEP/NCAR 40-Year Reanalysis Project, Bulletin of the American Meteorological Society, 77, 437–471, 1996.

Key, R. M., Kozyr, A., Sabine, C. L., Lee, K., Wanninkhof, R., Bullister, J. L., . . . Peng, T.-H.: A global ocean carbon climatology: Results from Global Data Analysis Project (GLODAP), Global Biogeochemical Cycles, 18, https://doi.org/10.1029/2004GB002247, 2004.

Kovaltsov, G. A., and Usoskin, I. G.: A new 3D numerical model of cosmogenic nuclide ^{10}Be production in the atmosphere, Earth and Planetary Science Letters, 291, 182–188, 2010.

Krakauer, N. Y., Randerson, J. T., Primeau, F. W., Gruber, N., and Menemenlis, D.: Carbon isotope evidence for the latitudinal distribution and wind speed dependence of the air-sea gas transfer velocity, Tellus B: Chemical and Physical Meteorology, 58, 390–417, 2006.

Kukla, G., and Robinson, D.: Annual Cycle of Surface Albedo, Monthly Weather Review, 108, 56–68, 1980.

Laj, C., Kissel, C., Mazaud, A., Channell, J. E., and Beer, J.: North Atlantic palaeointensity stack since 75ka (NAPIS-75) and the duration of the Laschamp event, Philosophical Transactions of the Royal Society of London. Series A: Mathematical, Physical and Engineering Sciences, 358, 1009–1025, 2000.

Laj, C., Kissel, C., Mazaud, A., Michel, E., Muscheler, R., and Beer, J.: Geomagnetic field intensity, North Atlantic Deep Water circulation and atmospheric $\Delta^{14}C$ during the last 50 kyr, Earth and Planetary Science Letters, 200, 177-190, 2002.

Laj, C., Kissel, C., and Beer, J.: High resolution global paleointensity stack since 75 kyr (GLOPIS-75) calibrated to absolute values, Timescales of the Paleomagnetic Field, 145, 255–265, 2004.

Laj, C., Guillou, H., and Kissel, C.: Dynamics of the earth magnetic field in the 10-75 kyr period comprising the Laschamp and Mono Lake excursions: New results from the French Chaîne des Puys in a global perspective, Earth and Planetary Science Letters, 387, 184–197, 2014.

Lisiecki, L. E., and Stern, J. V.: Regional and global benthic δ18O stacks for the last glacial cycle, Paleoceanography, 31, 1368–1394, 2016.

https://doi.org/10.5194/cp-2019-159
Preprint. Discussion started: 14 January 2020

Müller, J., and Stein, R.: High-resolution record of late glacial and deglacial sea ice changes in Fram Strait corroborates ice–ocean interactions during abrupt climate shifts, Earth and Planetary Science Letters, 403, 446–455, 2014.

Müller, S. A., Joos, F., Edwards, N. R., and Stocker, T. F.: Water Mass Distribution and Ventilation Time Scales in a Cost-Efficient, Three-Dimensional Ocean Model, Journal of Climate, 19, 5479–5499, 2006.

Müller, S. A., Joos, F., Plattner, G.-K., Edwards, N. R., and Stocker, T. F.: Modeled natural and excess radiocarbon: Sensitivities to the gas exchange formulation and ocean transport strength, Global Biogeochemical Cycles, 22, https://doi.org/10.1029/2007GB003065, 2008.

Marchal, O., Stocker, T. F., and Muscheler, R.: Atmospheric radiocarbon during the Younger Dryas: production, ventilation, or both?, Earth and Planetary Science Letters, 185, 383–395, 2001.

Mariotti, V., Paillard, D., Bopp, L., Roche, D. M., and Bouttes, N.: A coupled model for carbon and radiocarbon evolution during the last deglaciation, Geophysical Research Letters, 43, 1306–1313, 2016.

Masarik, J., and Beer, J.: Simulation of particle fluxes and cosmogenic nuclide production in the Earth's atmosphere, Journal of Geophysical Research: Atmospheres, 104, 12099–12111, 1999.

Masarik, J., and Beer, J.: An updated simulation of particle fluxes and cosmogenic nuclide production in the Earth's atmosphere, Journal of Geophysical Research: Atmospheres, 114, https://doi.org/10.1029/2008JD010557, 2009.

Menviel, L., Joos, F., and Ritz, S. P.: Simulating atmospheric CO_2, ^{13}C and the marine carbon cycle during the Last Glacial–Interglacial cycle: possible role for a deepening of the mean remineralization depth and an increase in the oceanic nutrient inventory, Quaternary Science Reviews, 56, 46–68, 2012.

Muscheler, R., and Heikkilä, U.: Constraints on long-term changes in solar activity from the range of variability of cosmogenic radionuclide records, Astrophysics and Space Sciences Transactions, 7, 355–364, 2011.

Muscheler, R., Beer, J., Wagner, G., Laj, C., Kissel, C., Raisbeck, G. M., . . . Kubike, P. W.: Changes in the carbon cycle during the last deglaciation as indicated by the comparison of ^{10}Be and ^{14}C records, Earth and Planetary Science Letters, 219, 325–340, 2004.

Muscheler, R., Adolphi, F., Herbst, K., and Nilsson, A.: The Revised Sunspot Record in Comparison to Cosmogenic Radionuclide-Based Solar Activity Reconstructions, Solar Physics, 291, 3025–3043, 2016.

Nowaczyk, N. R., Arz, H. W., Frank, U., Kind, J., and Plessen, B.: Dynamics of the Laschamp geomagnetic excursion from Black Sea sediments, Earth and Planetary Science Letters, 351-352, 54–69, 2012.

Nowaczyk, N. R., Frank, U., Kind, J., and Arz, H. W.: A high-resolution paleointensity stack of the past 14 to 68 ka from Black Sea sediments, Earth and Planetary Science Letters, 384, 1–16, 2013.

Orr, J. C., Najjar, R. G., Aumont, O., Bopp, L., Bullister, J. L., Danabasoglu, G., . . . Yool, A.: Biogeochemical protocols and diagnostics for the CMIP6 Ocean Model Intercomparison Project (OMIP), Geoscientific Model Development, 10, 2169–2199, 2017.

Parekh, P., Joos, F., and Müller, S. A.: A modeling assessment of the interplay between aeolian iron fluxes and iron-binding ligands in controlling carbon dioxide fluctuations during Antarctic warm events, Paleoceanography and Paleoclimatology, 23, https://doi.org/10.1029/2007PA001531, 2008.

https://doi.org/10.5194/cp-2019-159
Preprint. Discussion started: 14 January 2020

Peltier, W. R.: Ice Age Paleotopography, Science, 265, 195–201, 1994.

Poluianov, S. V., Kovaltsov, G. A., Mishev, A. L., and Usoskin, I. G.: Production of cosmogenic isotopes ^{7}Be, ^{10}Be, ^{14}C, ^{22}Na, and ^{36}Cl in the atmosphere: Altitudinal profiles of yield functions, Journal of Geophysical Research: Atmospheres, 121, 8125–8136, 2016.

Potgieter, M. S., Vos, E. E., Boezio, M., De Simone, N., Di Felice, V., and Formato, V.: Modulation of Galactic Protons in the Heliosphere During the Unusual Solar Minimum of 2006 to 2009, Solar Physics, 289, 391–406, 2014.

Raisbeck, G. M., Cauquoin, A., Jouzel, J., Landais, A., Petit, J.-R., Lipenkov, V. Y., . . . Yiou, F.: An improved north-south synchronization of ice core records around the 41 kyr ^{10}Be peak, Climate of the Past, 13, 217–229, 2017.

Rasmussen, S. O., Abbott, P. M., Blunier, T., Bourne, A. J., Brook, E. J., Buchardt, S. L., . . . Winstrup, M.: A first chronology for the North Greenland Eemian Ice Drilling (NEEM) ice core, Climate of the Past, 9, 2713–2730, 2013.

Reimer, P., Bard, E., Bayliss, A., Beck, J., Blackwell, P., Ramsey, C., . . . Van der Plicht, J.: IntCal13 and Marine13 Radiocarbon Age Calibration Curves 0-50,000 Years cal BP, Radiocarbon, 55, 1869–1887, 2013.

Ritz, S. P., Stocker, T. F., and Joos, F.: A Coupled Dynamical Ocean–Energy Balance Atmosphere Model for Paleoclimate Studies, Journal of Climate, 24, 349–375, 2011.

Roth, R., and Joos, F.: A reconstruction of radiocarbon production and total solar irradiance from the Holocene ^{14}C and CO_2 records: implications of data and model uncertainties, Climate of the Past, 9, 1879–1909, 2013.

Roth, R., Ritz, S. P., and Joos, F.: Burial-nutrient feedbacks amplify the sensitivity of atmospheric carbon dioxide to changes in organic matter remineralisation, Earth System Dynamics, 5, 321–343, 2014.

Sarnthein, M., Schneider, B., and Grootes, P. M.: Peak glacial ^{14}C ventilation ages suggest major draw-down of carbon into the abyssal ocean, Climate of the Past, 9, 2595–2614, 2013.

Siegenthaler, U., and Oeschger, H.: Biospheric CO_2 emissions during the past 200 years reconstructed by deconvolution of ice core data, Tellus, 39B, 140–154, 1987.

Siegenthaler, U., Heimann, M., and Oeschger, H.: ^{14}C Variations Caused by Changes in the Global Carbon Cycle, Radiocarbon, 22, 177–191, 1980.

Skinner, L. C., Fallon, S., Waelbroeck, C., Michel, E., and Barker, S.: Ventilation of the Deep Southern Ocean and Deglacial CO_2 Rise, Science, 328, 1147–1151, 2010.

Skinner, L. C., Primeau, F., Freeman, E., de la Fuente, M., Goodwin, P. A., Gottschalk, J., . . . Scrivner, A. E.: Radiocarbon constraints on the glacial ocean circulation and its impact on atmospheric CO_2, Nature Communications, 8, 16010, 2017.

Soulet, G., Skinner, L. C., Beaupré, S. R., and Galy, V.: A Note on Reporting of Reservoir ^{14}C Disequilibria and Age Offsets, Radiocarbon, 58, 205–211, 2016.

Southon, J., Noronha, A. L., Cheng, H., Edwards, R. L., and Wang, Y.: A high-resolution record of atmospheric ^{14}C based on Hulu Cave speleothem H82, Quaternary Science Reviews, 33, 32–41, 2012.

Stuiver, M., and Polach, H. A.: Discussion: Reporting of ^{14}C Data, Radiocarbon, 19, 355–363, 1977.

https://doi.org/10.5194/cp-2019-159
Preprint. Discussion started: 14 January 2020

Climate of the Past Discussions

Tschumi, T., Joos, F., and Parekh, P.: How important are Southern Hemisphere wind changes for low glacial carbon dioxide? A model study, Paleoceanography and Paleoclimatology, 23, https://doi.org/10.1029/2008PA001592, 2008.

Tschumi, T., Joos, F., Gehlen, M., and Heinze, C.: Deep ocean ventilation, carbon isotopes, marine sedimentation and the deglacial CO_2 rise, Climate of the Past, 7, 771–800, 2011.

Usoskin, I. G., Hulot, G., Gallet, Y., Roth, R., Licht, A., Joos, F., . . . Khokhlov, A.: Evidence for distinct modes of solar activity, Astronomy & Astrophysics, 562, 1–4, 2014.

Wagner, G., Beer, J., Masarik, J., Muscheler, R., Kubik, P. W., Mende, W., . . . Yiou, F.: Presence of the solar de Vries cycle (~205 years) during the last ice age, Geophysical Research Letters, 28, 303–306, 2001.

Wallmann, K., Schneider, B., and Sarnthein, M.: Effects of eustatic sea-level change, ocean dynamics, and nutrient utilization on atmospheric pCO_2 and seawater composition over the last 130 000 years: a model study, Climate of the Past, 12, 339–375, 2016.

Yiou, F., Raisbeck, G. M., Baumgartner, S., Beer, J., Hammer, C., Johnsen, S., . . . Yiou, P.: Beryllium 10 in the Greenland Ice Core Project ice core at Summit, Greenland, Journal of Geophysical Research: Oceans, 102, 26783–26794, 1997.

https://doi.org/10.5194/cp-2019-159
Preprint. Discussion started: 14 January 2020

Climate of the Past
Discussions
Open Access
EGU

Table 1. Summary of model scenarios considered in this study. Initial conditions refer to the boundary conditions used for the precursor spin-up simulation needed to initialize the transient simulation. These correspond either to preindustrial (PI) or last glacial conditions. The paleoclimate forcing fields, i.e., Orb-GHG-Ice, are reconstructed changes in orbital parameters (Berger, 1978), greenhouse gas radiative forcing based on reconstructed atmospheric greenhouse gas histories (Köhler et al., 2017), and varying ice sheet extent scaled using the global benthic δ^{18}O stack of Lisiecki and Stern (2016). Numbers refer to the scale factor values applied to the tunable model parameters τ (wind stress scale factor), K_V (vertical diffusivity), k_w (gas transfer velocity), rr ($CaCO_3$-to-POC export ratio), and ℓ_{POC} (POC remineralization length scale) at the last glacial maximum (LGM). These values were chosen in order to achieve an atmospheric CO_2 concentration close to the LGM level, and are varied over time using the global benthic δ^{18}O stack.

			Tunable parameters: scale factor at LGM				
Scenario	Initial conditions	Paleoclimate forcing	τ	K_V	k_w	rr	ℓ_{POC}
MOD	PI	-	-	-	-	-	-
PAL	Glacial	Orb-GHG-Ice	-	-	-	-	-
CIRC	Glacial	Orb-GHG-Ice	0.4	0.4	-	-	-
VENT	Glacial	Orb-GHG-Ice	0.4	0.4	0.4	-	-
VENTx	Glacial	Orb-GHG-Ice	0.4	0.4	0.0	-	-
BIO	Glacial	Orb-GHG-Ice	-	-	-	0.8	1.2
PHYS-BIO	Glacial	Orb-GHG-Ice	0.7	0.7	0.7	0.7	-
PHYS-BIOx	Glacial	Orb-GHG-Ice	0.8	0.8	0.8	0.8	1.2

https://doi.org/10.5194/cp-2019-159
Preprint. Discussion started: 14 January 2020

Climate of the Past
Open Access
Discussions

Table 2. Production rate estimates in relative units inferred from three fundamentally different reconstruction methods: geomagnetic field data from marine sediments, ^{10}Be and ^{36}Cl measurements in polar ice cores, and model-based deconvolution of atmospheric $\Delta^{14}C$. Laj00, Laj04, Now13, and Chn18 refer to the paleointensity-based reconstructions of Laj et al. (2000), Laj et al. (2004), Nowaczyk et al. (2013), and Channell et al. (2018), respectively. Adp18 refers to the ice-core ^{10}Be-based reconstruction of Adolphi et al. (2018). Int13 and Hul18 refer to the model-based reconstructions from this study, using the IntCal13 calibration curve (Reimer et al., 2013) and the new Hulu Cave $\Delta^{14}C$ dataset (Cheng et al., 2018). The bold numbers show the mean production rates during the last glacial (50 to 18 kyr BP).

	Mean production rate (relative units)						
Time (kyr BP)	Laj00	Laj04	Now13	Chn18	Adp18	Int13	Hul18
50 to 42	1.08	1.04	1.12	1.08	1.01	1.23	1.14
42 to 37	1.57	1.56	1.71	1.36	1.44	1.45	1.67
37 to 32	1.19	1.09	1.35	0.98	1.10	1.25	1.28
32 to 22	1.22	1.15	1.29	0.92	0.99	1.31	1.31
22 to 18	1.31	1.20	1.17	0.81	0.98	1.11	1.11
50 to 18	**1.25**	**1.18**	**1.31**	**1.01**	**1.08**	**1.28**	**1.29**

https://doi.org/10.5194/cp-2019-159
Preprint. Discussion started: 14 January 2020

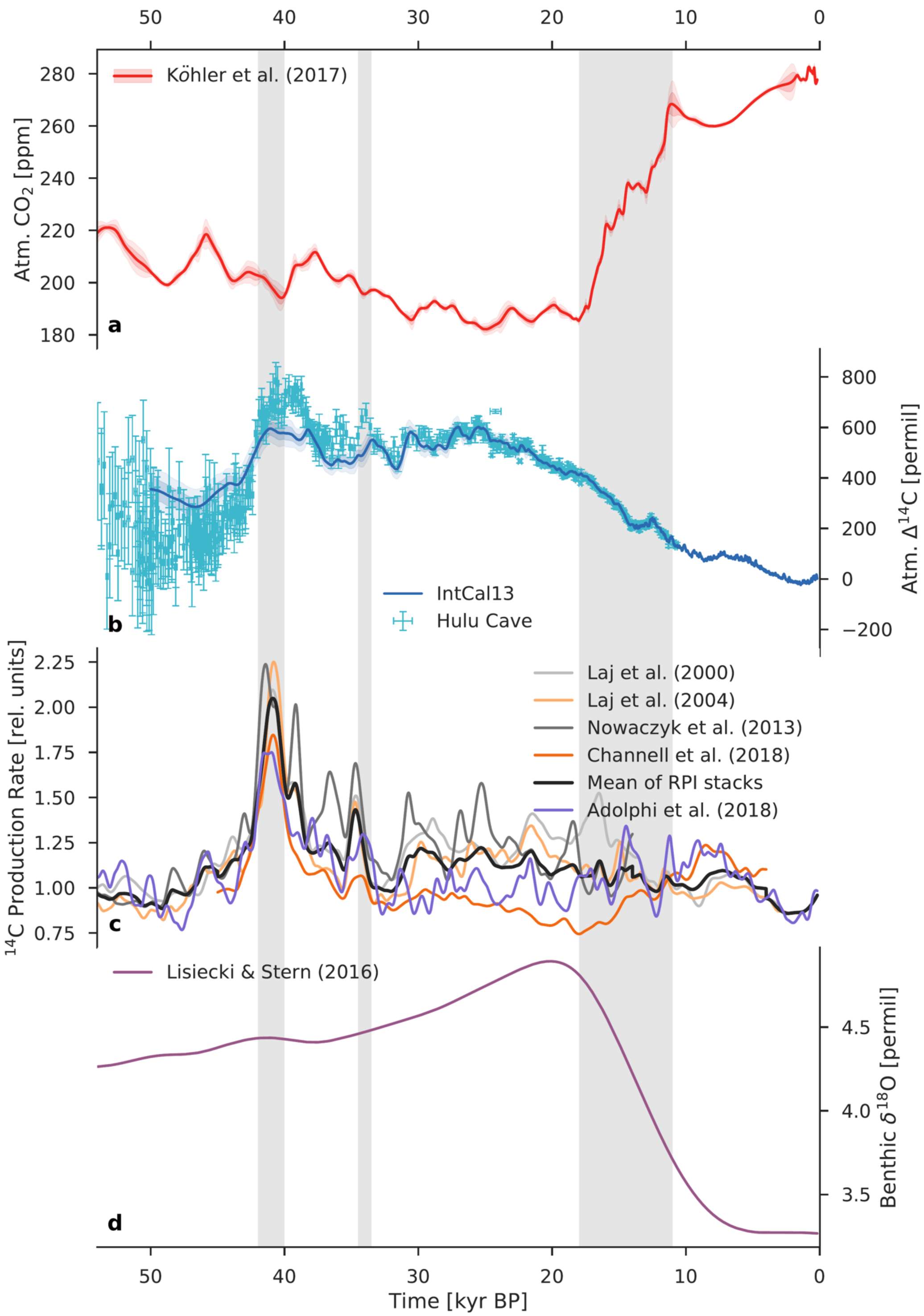

1071

https://doi.org/10.5194/cp-2019-159
Preprint. Discussion started: 14 January 2020

Climate of the Past
Discussions

Fig. 1. Comparison of various paleoclimate records for the last 54 kyr. (a) Atmospheric CO_2 from the data compilation of Köhler et al. (2017). The light red envelope shows the uncertainty (2σ). (b) Atmospheric $\Delta^{14}C$ reconstructed from ^{14}C measurements on tree rings, plant macrofossils, speleothems, corals, and foraminifera. The light blue envelope shows the uncertainty (2σ) in the IntCal13 calibration curve (Reimer et al., 2013), whereas the Hulu Cave data (Cheng et al., 2018) are shown with error bars (1σ). Hulu Cave data are consistent with IntCal13 between ~10.6 and 33.3 kyr BP. For both records $\Delta^{14}C$ values were adjusted to the presently accepted value of the radiocarbon half-life (5700 years). (c) ^{14}C production rate in relative units reconstructed from paleointensity data (Laj et al., 2000; Laj et al., 2004; Nowaczyk et al., 2013; Channell et al., 2018) and from polar ice-core ^{10}Be fluxes (Adolphi et al., 2018). The heavy dark gray line is the mean paleointensity-based ^{14}C production rate. (d) Global benthic $\delta^{18}O$ stack, a proxy for ice volume, from Lisiecki and Stern (2016). Three vertical light gray bars indicate the Laschamp excursion (~41 kyr BP), when the Earth's geomagnetic dipole field intensity was close to zero, the Mono Lake geomagnetic excursion (~34 kyr BP), and the last glacial termination (~18 to 11 kyr BP), respectively.

https://doi.org/10.5194/cp-2019-159
Preprint. Discussion started: 14 January 2020

Climate of the Past Discussions

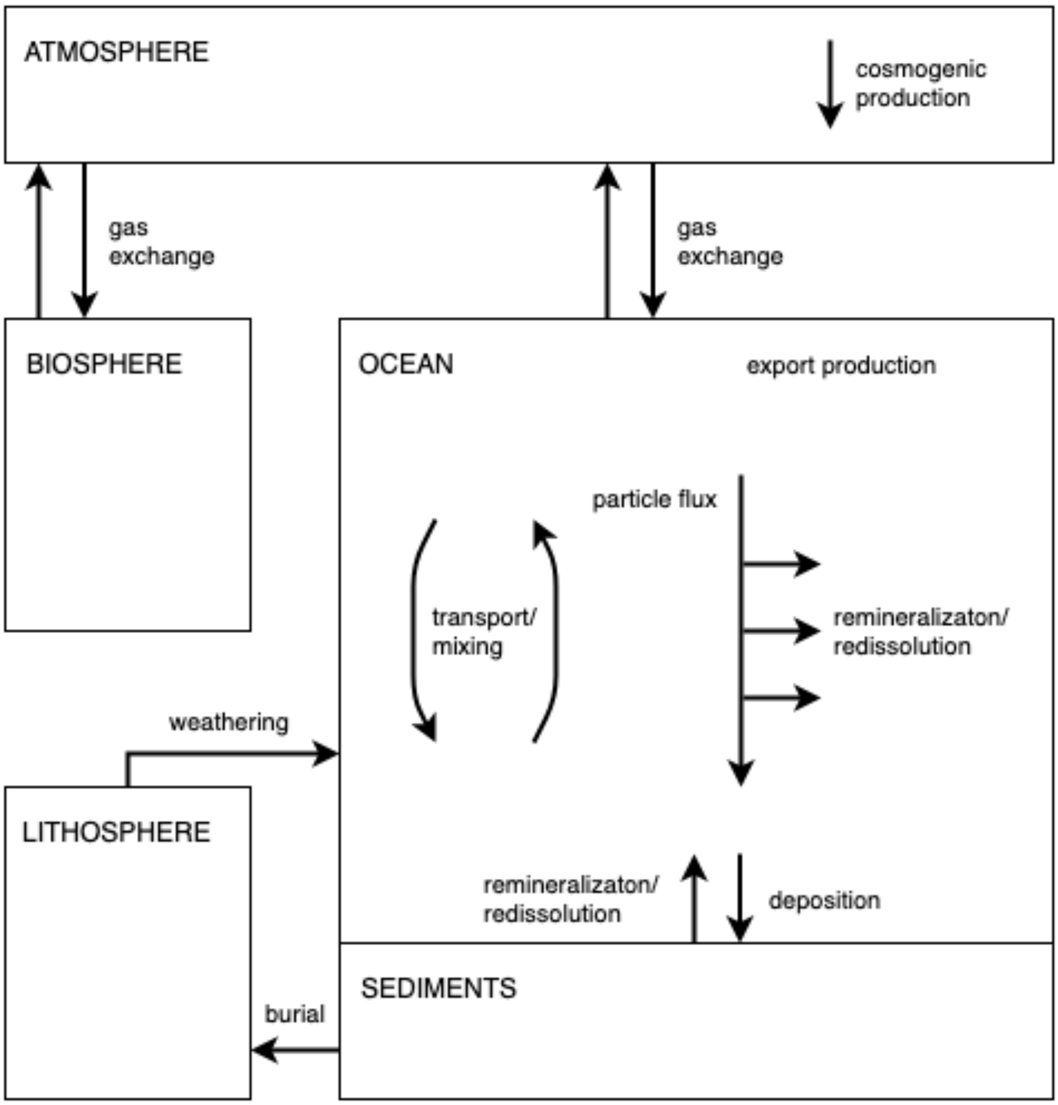

Fig. 2. Schematic diagram of the Bern3D carbon cycle model. The fully coupled model includes the major global carbon reservoirs (atmosphere, terrestrial biosphere, ocean, and sediments) and the exchange fluxes between them. Biogeochemical processes, namely, air-sea gas exchange, biological export production, and particle flux through the water column, are parameterized by refined OCMIP-2 formulations. Details concerning the model are provided in Sect. 2 and Appendix A.

https://doi.org/10.5194/cp-2019-159
Preprint. Discussion started: 14 January 2020

Climate of the Past Discussions
Open Access

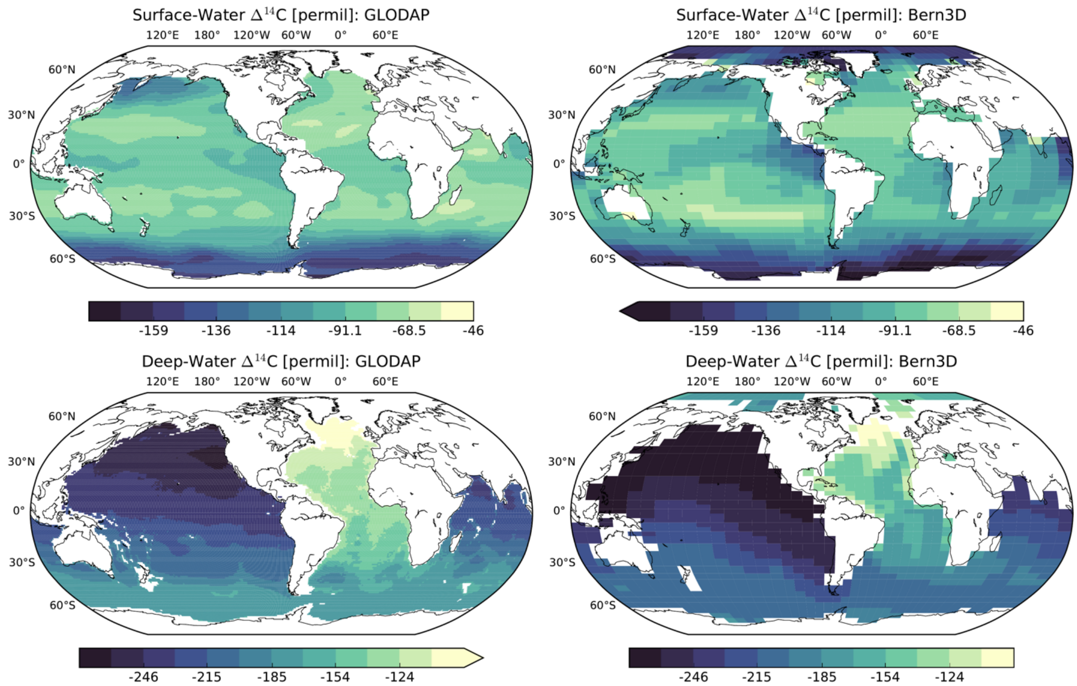

Fig. 3. Steady-state distribution of $\Delta^{14}C$ in the surface (> 100 m) and deep (< 1500 m) ocean for the preindustrial control run (right), compared to the distribution of $\Delta^{14}C$ based on the Global Ocean Data Analysis Project (GLODAP).

https://doi.org/10.5194/cp-2019-159
Preprint. Discussion started: 14 January 2020

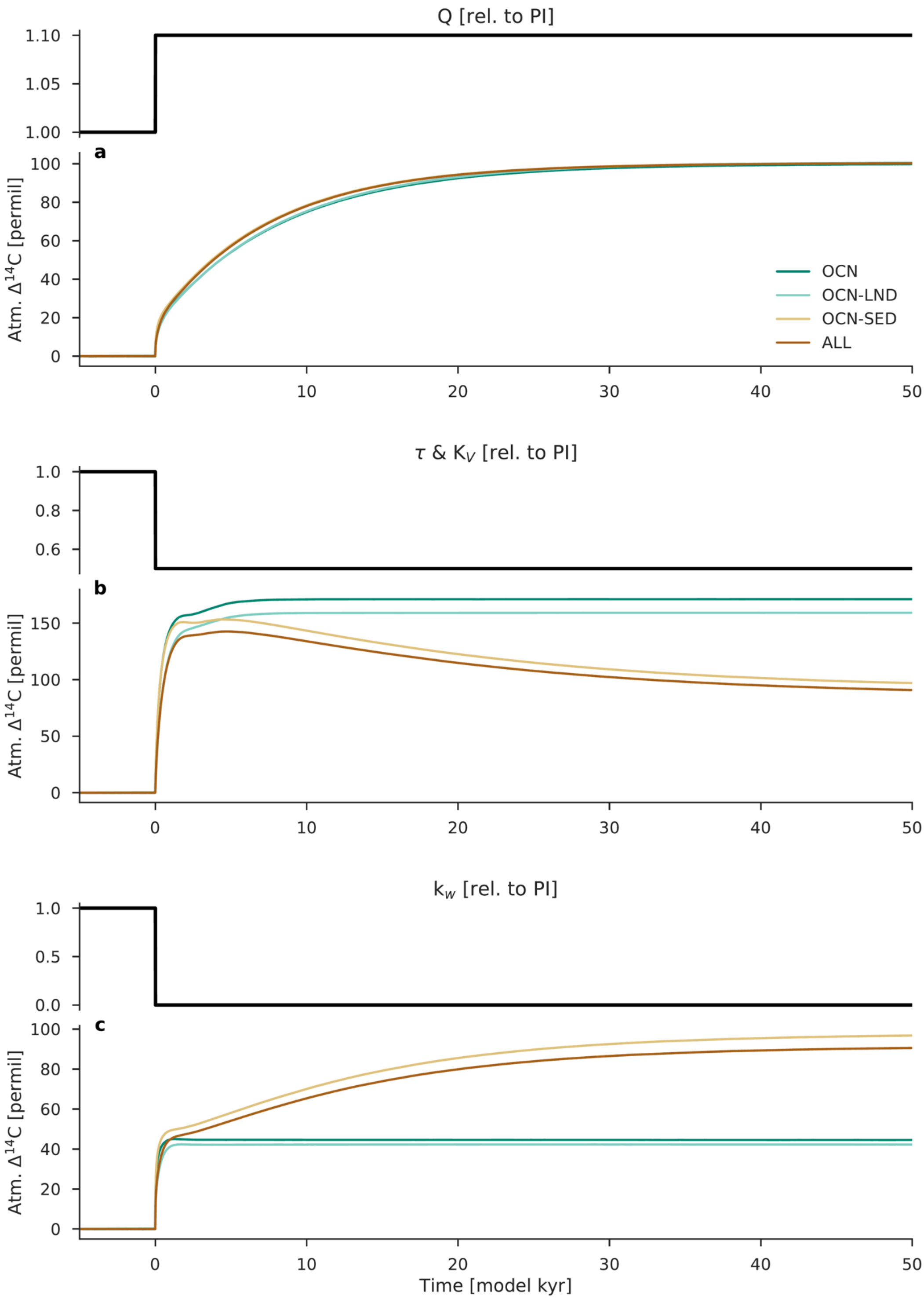

1129

https://doi.org/10.5194/cp-2019-159
Preprint. Discussion started: 14 January 2020

Climate of the Past
Discussions

Fig. 4. Response of atmospheric $\Delta^{14}C$ to step changes in ^{14}C production, followed by step changes in the tunable model parameters of the ocean carbon cycle. (a) ^{14}C production Q is increased at time 0 from 100 to 110 percent of its preindustrial value ("higher production" scenario). (b) Wind stress scale factor τ and vertical diffusivity K_V are decreased at time 0 from 100 to 50 percent of their preindustrial values ("reduced deep ocean ventilation" scenario). (c) Gas transfer velocity k_w is decreased at time 0 from 100 to 0 percent of its preindustrial value at the north (> 60°N) and south (> 48°S) poles ("enhanced permanent sea ice cover" scenario). Four model configurations are considered. The dark turquoise line shows the model results using the atmosphere–ocean (OCN) configuration, the light turquoise line is the atmosphere–ocean–land (OCN-LND) configuration, the light brown line is the atmosphere–ocean–sediment (OCN-SED) configuration, and the dark brown line is the atmosphere–ocean–land–sediment (ALL) configuration.

https://doi.org/10.5194/cp-2019-159
Preprint. Discussion started: 14 January 2020

Climate of the Past
Discussions

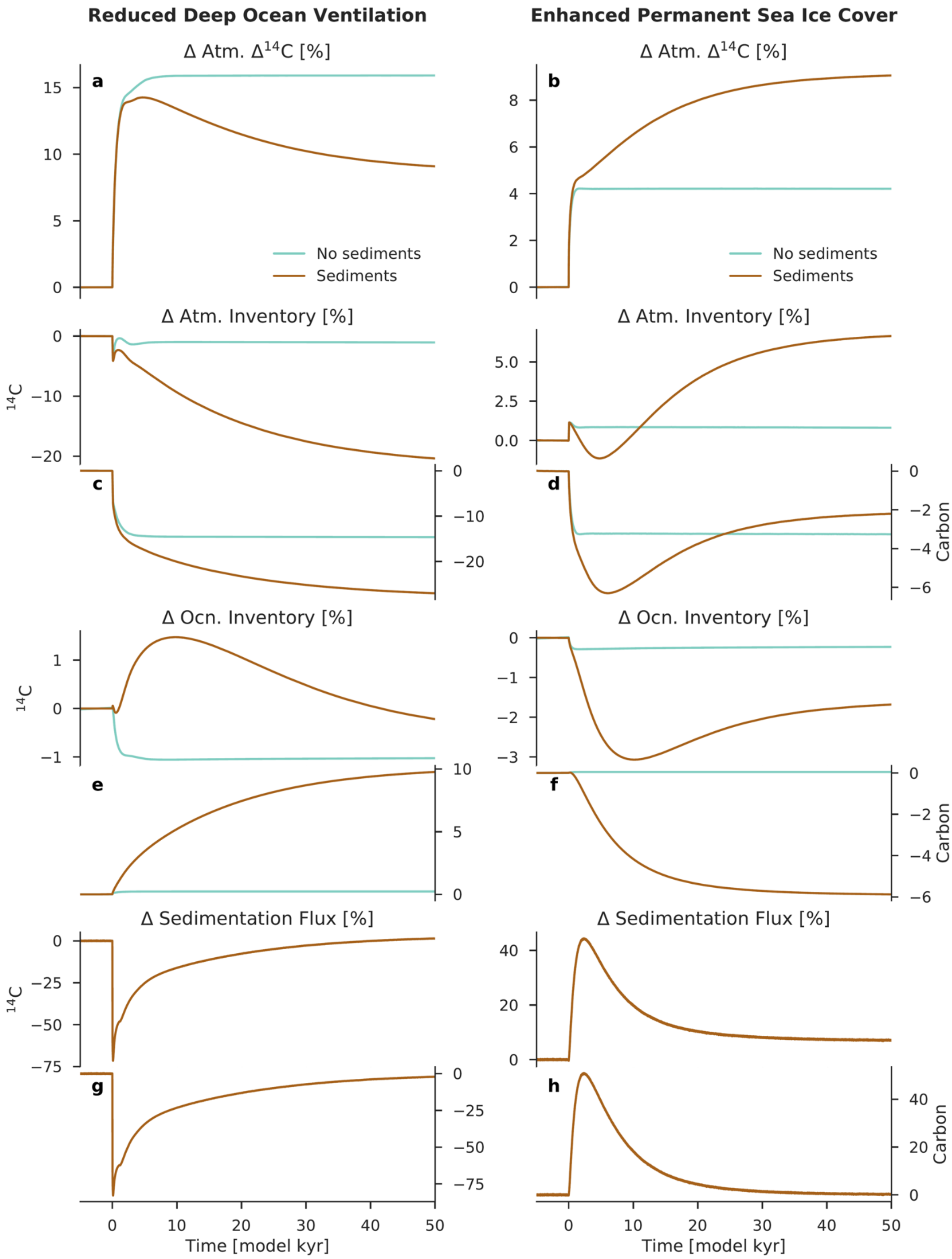

1159

https://doi.org/10.5194/cp-2019-159
Preprint. Discussion started: 14 January 2020

Fig. 5. Changes in carbon reservoir sizes and the sedimentation flux for the scenarios “reduced deep ocean ventilation” (left) and “enhanced permanent sea ice cover” (right). The change in atmospheric $\Delta^{14}C$ is also shown (a, b). Anomalies are expressed here as differences relative to the preindustrial steady state (in percent). Turquoise lines show the model results using configuration OCN-LND (no sediments) and brown lines are configuration ALL (model includes sediments). The y-axis on the left-hand side of each panel refers to changes in the ^{14}C inventory, whereas the y-axis on the right-hand side of each panel refers to changes in the carbon inventory or flux.

https://doi.org/10.5194/cp-2019-159
Preprint. Discussion started: 14 January 2020

Climate of the Past
Discussions

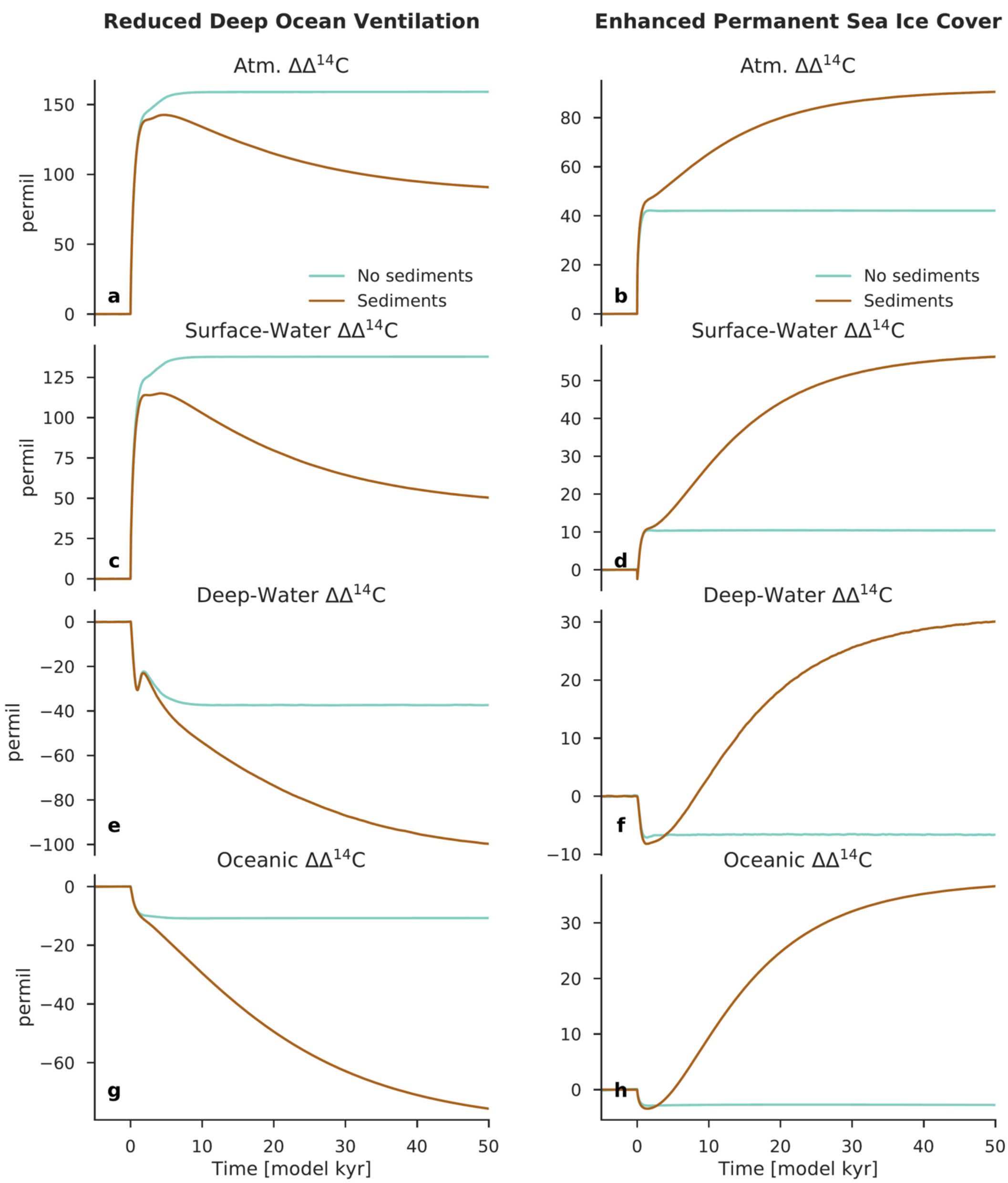

Fig. 6. Change in $\Delta^{14}C$ for the atmosphere, surface ocean, deep ocean, and global ocean for the scenarios "reduced deep ocean ventilation" (left) and "enhanced permanent sea ice cover" (right). Anomalies are expressed here as differences relative to the preindustrial steady state (in permil). Turquoise lines show the model results using configuration OCN-LND (no sediments) and brown lines are configuration ALL (model includes sediments).

https://doi.org/10.5194/cp-2019-159
Preprint. Discussion started: 14 January 2020

Climate of the Past
Discussions
Open Access

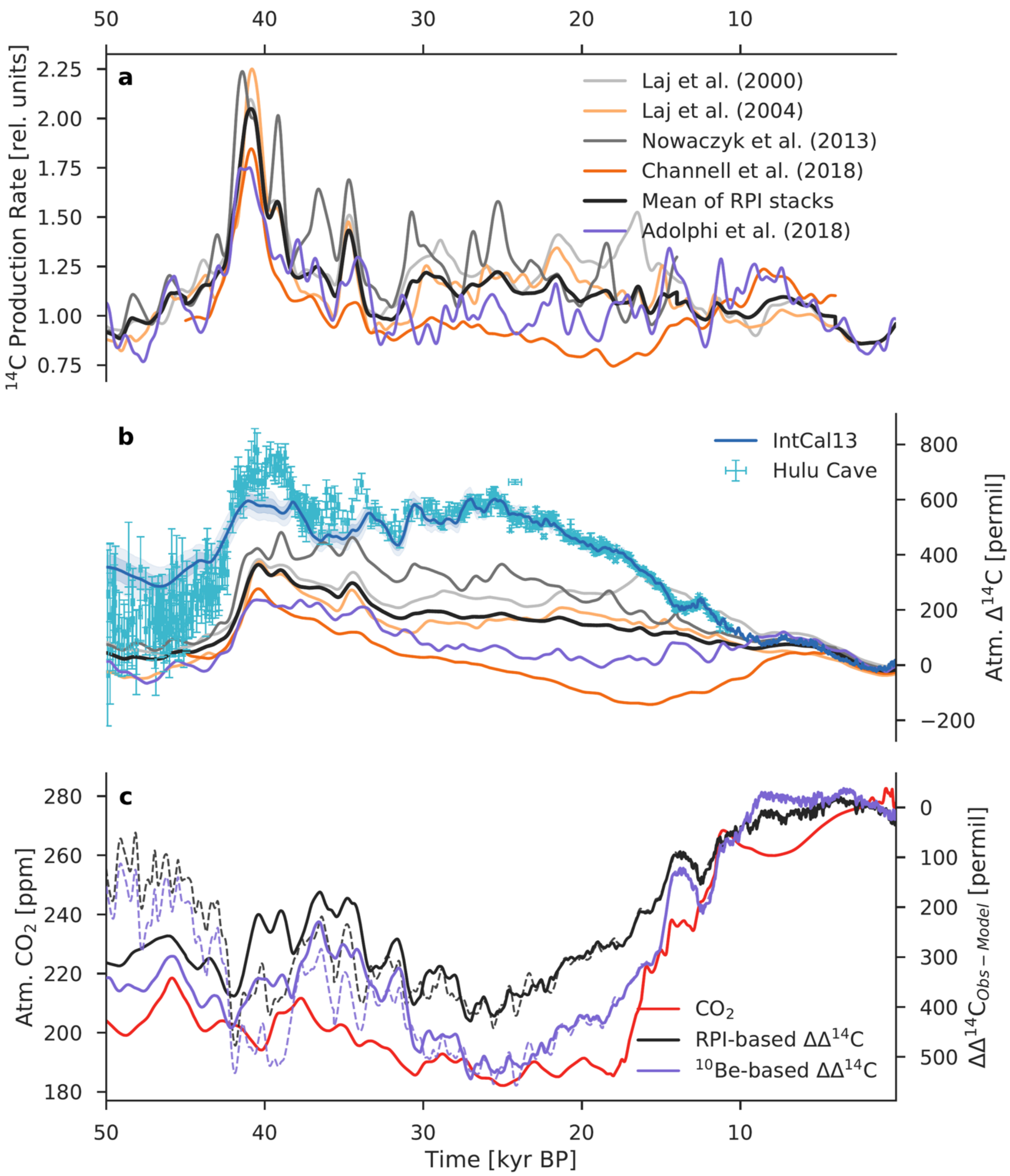

Fig. 7. Component of atmospheric Δ^{14}C variability caused by production changes alone. (a) Relative ^{14}C production rate as inferred from paleointensity data (gray) and from polar ice-core ^{10}Be fluxes (purple). The heavy dark gray line is the mean paleointensity-based ^{14}C production rate. (b) Modelled Δ^{14}C records based only on ^{14}C production changes, compared with the reconstructed IntCal13 and Hulu Cave Δ^{14}C records. The modelled records are given by scenario MOD that assumes a constant preindustrial carbon cycle. (c) Difference between reconstructed Δ^{14}C and model-simulated Δ^{14}C using paleointensity data (RPI-based $\Delta\Delta^{14}$C; gray) and ice-core ^{10}Be data (^{10}Be-based $\Delta\Delta^{14}$C; purple),

https://doi.org/10.5194/cp-2019-159
Preprint. Discussion started: 14 January 2020

compared with the atmospheric CO_2 record (red). Solid lines show the IntCal13–model difference, whereas dashed lines show the Hulu–model difference. The $\Delta\Delta^{14}C$ curve indicates changes in $\Delta^{14}C$ that can be attributed to some combination of carbon cycle changes, uncertainties in the reconstruction of the ^{14}C production rate, and uncertainties in the IntCal13 and Hulu Cave $\Delta^{14}C$ records.

Climate of the Past
Discussions

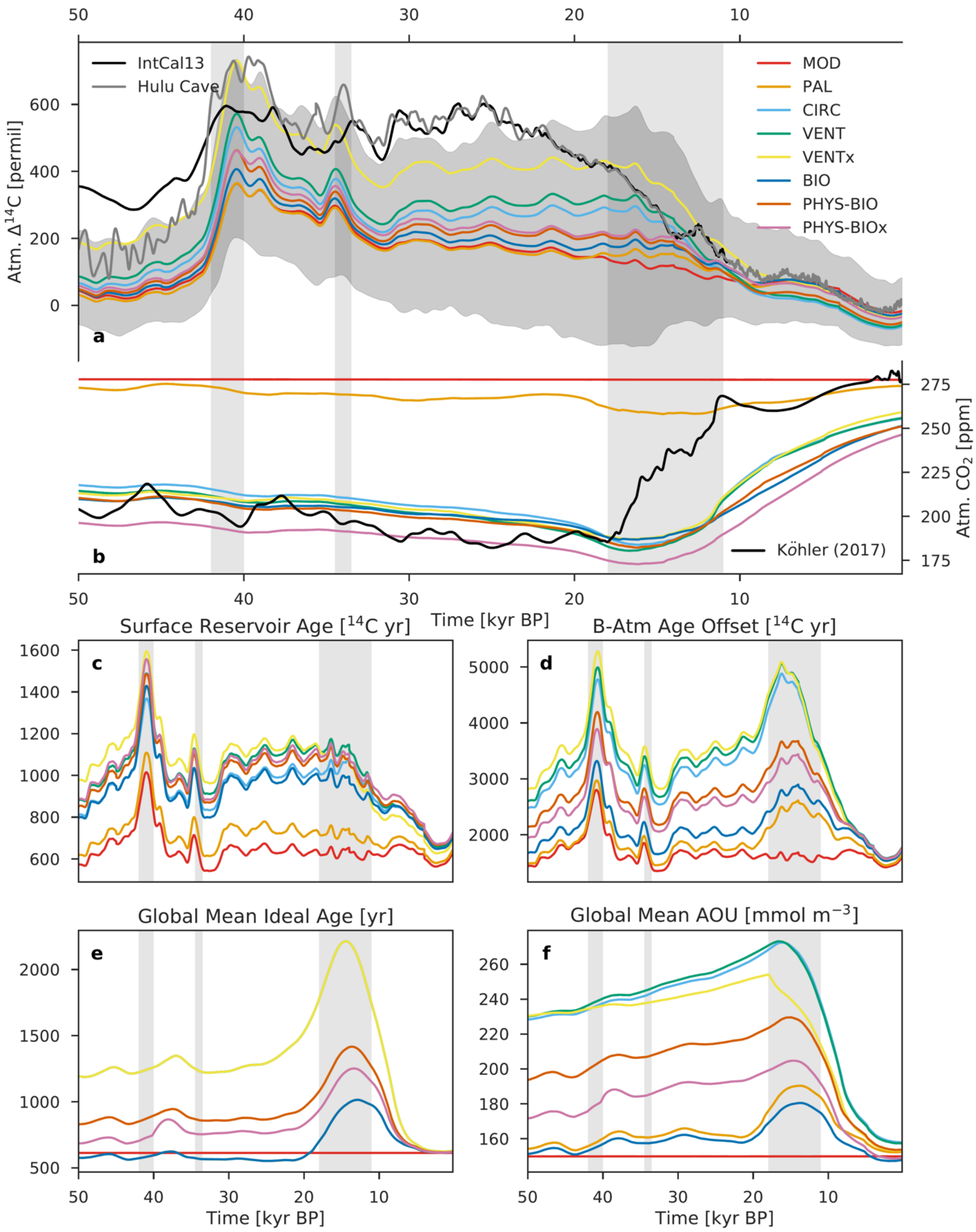

Fig. 8. Modelled records of atmospheric (a) $\Delta^{14}C$ and (b) CO_2, compared with their reconstructed atmospheric histories (black and gray lines). Also shown are modelled records of (c) surface reservoir age, (d) B-Atm ^{14}C age offset, (e) ideal age, and (f) apparent oxygen utilization (AOU). Colored lines show the results of model runs using the mean

https://doi.org/10.5194/cp-2019-159
Preprint. Discussion started: 14 January 2020

paleointensity-based ^{14}C production rate and the eight different carbon cycle scenarios described in Sect. 2.4 and Table 1. The gray envelope in (a) shows the uncertainty (2σ) from all production rate reconstructions and carbon cycle scenarios, providing a bounded estimate of $\Delta^{14}C$ change. Radiocarbon ventilation ages are expressed here as radiocarbon reservoir age offsets following Soulet et al. (2016) which are used extensively by the radiocarbon dating community.

https://doi.org/10.5194/cp-2019-159
Preprint. Discussion started: 14 January 2020

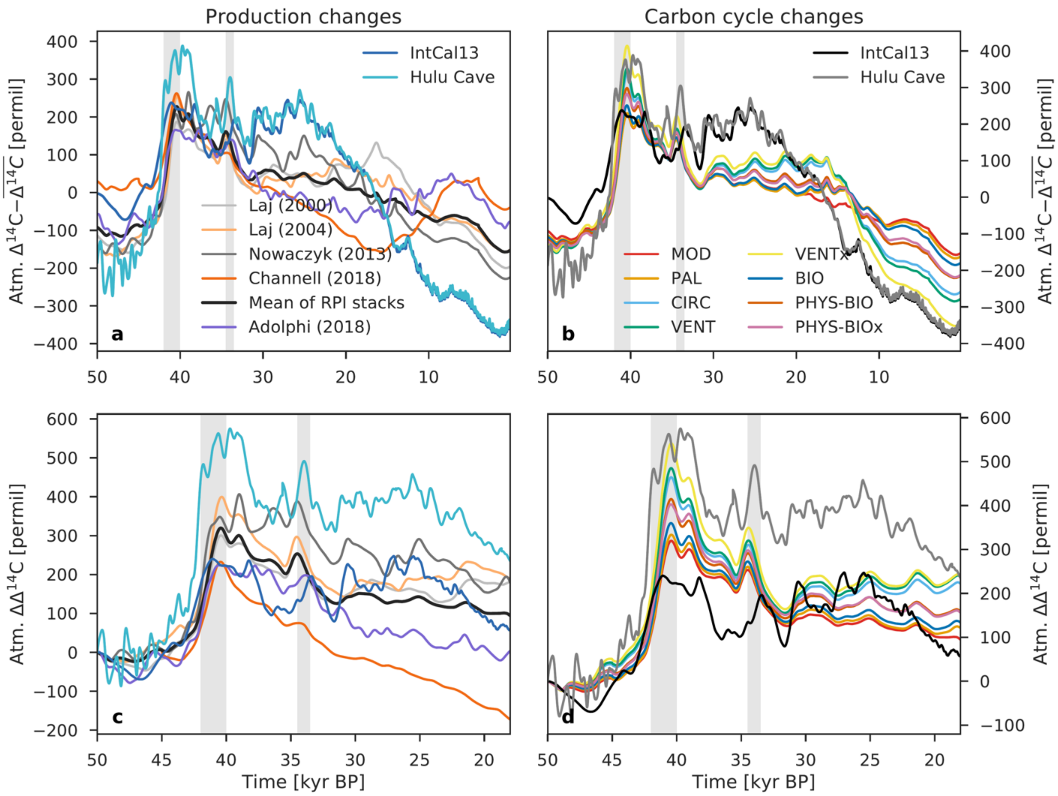

Fig. 9. Comparison of atmospheric $\Delta^{14}C$ variability caused by changes in the ocean carbon cycle (b, d) with production-driven changes in atmospheric $\Delta^{14}C$ using scenario MOD (a, c). For the analysis of carbon cycle changes, only the results of model runs using the mean paleointensity-based ^{14}C production rate are shown. The $\Delta^{14}C$ records in the upper panel (a, b) have been detrended to remove the mean, whereas the lower panel (c, d) shows $\Delta^{14}C$ anomalies expressed as differences relative to the $\Delta^{14}C$ value at 50 kyr BP, only for the portion of the record older than 18 kyr BP. Two vertical light gray bars indicate the Laschamp (~41 kyr BP) and Mono Lake (~34 kyr BP) geomagnetic excursions.

https://doi.org/10.5194/cp-2019-159
Preprint. Discussion started: 14 January 2020

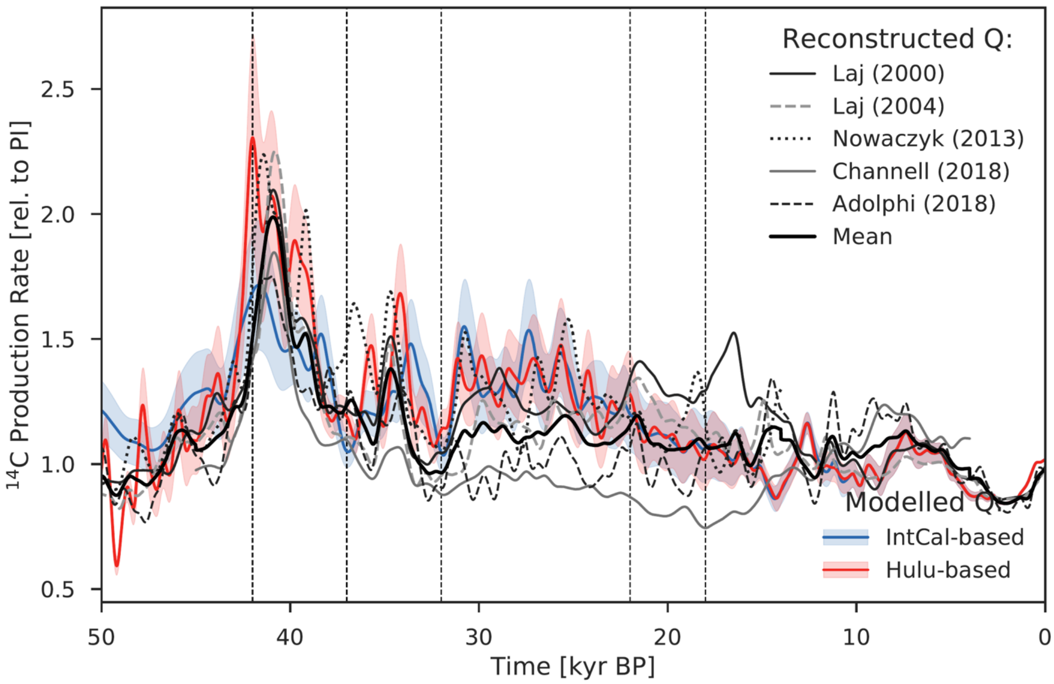

Fig. 10. Model-based ^{14}C production rate in relative units compared with paleointensity-based and ice-core ^{10}Be-based estimates. Here, the ^{14}C production rate is inferred from an atmospheric radiocarbon budget, using the Bern3D carbon cycle model forced with reconstructed variations in atmospheric $\Delta^{14}C$ and CO_2. Results of model runs using the IntCal13 calibration curve and seven carbon cycle scenarios are shown in the light blue envelope (2σ). The light red envelope (2σ) shows the results obtained using the composite Hulu Cave (10.6 to 50 kyr BP) and IntCal13 (0 to 10.6 kyr BP) $\Delta^{14}C$ record. The heavy black line is the mean of the five available production rate reconstructions: Laj et al. (2000), Laj et al. (2004), Nowaczyk et al. (2013), Channell et al. (2018), and Adolphi et al. (2018).

https://doi.org/10.5194/cp-2019-159
Preprint. Discussion started: 14 January 2020

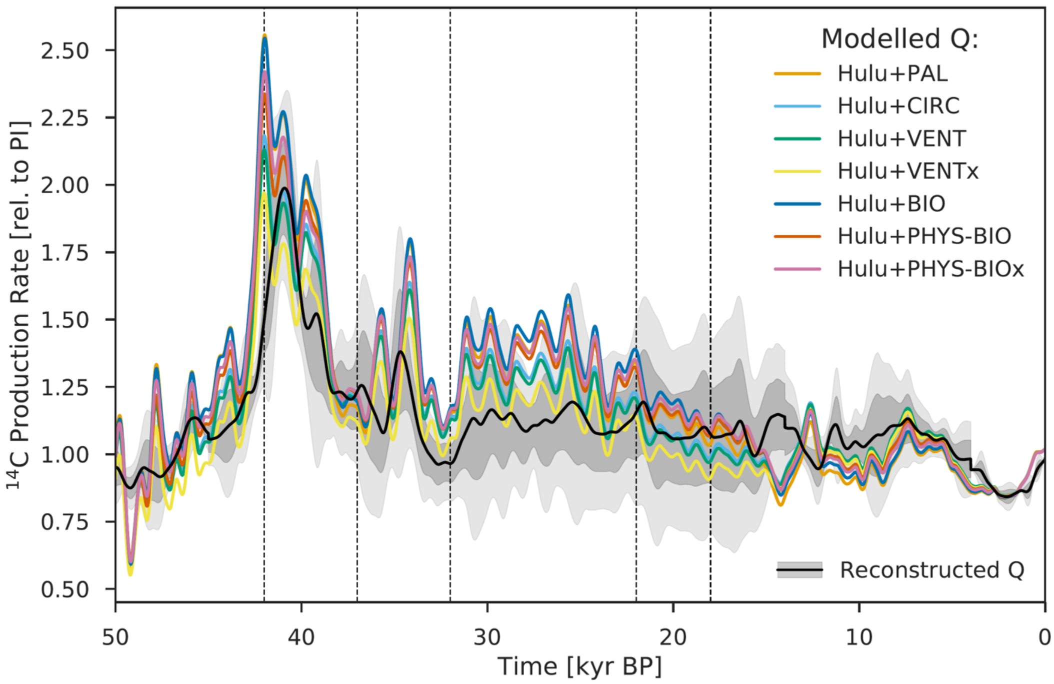

Fig. 11. Relative ^{14}C production rate as inferred from the Bern3D model under seven carbon cycle scenarios (see Sect. 2.4). Estimates shown here are obtained by the composite Hulu Cave and IntCal13 $\Delta^{14}C$ record. The black line is the mean of the five available production rate reconstructions shown in Fig. 10; the gray envelope shows its uncertainty (2σ).